AD-A135 538 NONLINEAR MODE COUPLING THEORY OF THE LOWER-HYBRID-DRIFT INSTABILITY(U) NAVAL RESEARCH LAB WASHINGTON DC J F DRAKE ET AL. 25 NOV 83 NRL-MR-5209 1/1

UNCLASSIFIED F/G 12/1 NL

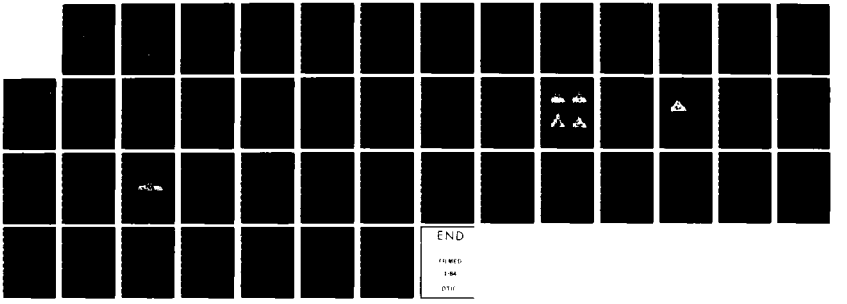

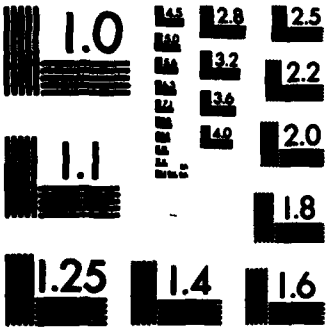

NRL Memorandum Report 5209

Nonlinear Mode Coupling Theory of the Lower-Hybrid-Drift Instability

J. F. DRAKE,* P. N. GUZDAR,** A. B. HASSAM** AND J. D. HUBA

Geophysical and Plasma Dynamics Branch
Plasma Physics Division

**University of Maryland*
College Park, MD 20742

***Science Applications, Inc.*
McLean, VA 22102

November 25, 1983

This research was supported by the Office of Naval Research and the National Aeronautics and Space Administration.

NAVAL RESEARCH LABORATORY
Washington, D.C.

SECURITY CLASSIFICATION OF THIS PAGE (When Data Entered)

REPORT DOCUMENTATION PAGE	READ INSTRUCTIONS BEFORE COMPLETING FORM
1. REPORT NUMBER NRL Memorandum Report 5209	2. GOVT ACCESSION NO. A135-538
3. RECIPIENT'S CATALOG NUMBER	
4. TITLE (and Subtitle) NONLINEAR MODE COUPLING THEORY OF THE LOWER-HYBRID-DRIFT INSTABILITY	5. TYPE OF REPORT & PERIOD COVERED Interim report on a continuing NRL problem.
	6. PERFORMING ORG. REPORT NUMBER
7. AUTHOR(s) J.F. Drake,* P.N. Guzdar,** A.B. Hassam** and J.D. Huba	8. CONTRACT OR GRANT NUMBER(s)
9. PERFORMING ORGANIZATION NAME AND ADDRESS Naval Research Laboratory Washington, DC 20375	10. PROGRAM ELEMENT, PROJECT, TASK AREA & WORK UNIT NUMBERS W-15494; 61153N; RR033-02-44; 47-1982-0-3; 47-0884-0-3
11. CONTROLLING OFFICE NAME AND ADDRESS Office of Naval Research National Aeronautics & Space Admin. Arlington, VA 22203 Washington, DC 20546	12. REPORT DATE November 25, 1983
	13. NUMBER OF PAGES 46
14. MONITORING AGENCY NAME & ADDRESS(if different from Controlling Office)	15. SECURITY CLASS. (of this report) UNCLASSIFIED
	15a. DECLASSIFICATION/DOWNGRADING SCHEDULE

16. DISTRIBUTION STATEMENT (of this Report)

Approved for public release; distribution unlimited.

17. DISTRIBUTION STATEMENT (of the abstract entered in Block 20, if different from Report)

18. SUPPLEMENTARY NOTES

*Present address: University of Maryland, College Park, MD 20742

**Present address: Science Applications, Inc., McLean, VA 22102

This research was supported by the Office of Naval Research and the National Aeronautics and Space Administration.

19. KEY WORDS (Continue on reverse side if necessary and identify by block number)

Lower-hybrid-drift instability
Nonlinear plasma theory
Magnetospheric physics
Ionospheric physics

beta,

A

20. ABSTRACT (Continue on reverse side if necessary and identify by block number)

A nonlinear mode coupling theory of the lower-hybrid-drift instability is presented. A two-dimensional nonlinear wave equation is derived which describes lower-hybrid-drift wave turbulence in the plane transverse to $\underline{B}$ ($\underline{k} \cdot \underline{B} = 0$), and which is valid for finite $\underline{E}$, collisional and collisionless plasmas. The instability saturates by transferring energy from growing, long wavelength modes to damped, short wavelength modes. Detailed numerical results are presented which compare favorably to both recent computer simulations and experimental observations. Applications of this theory to space plasmas, the earth's magnetotail and the equatorial F region ionosphere, are discussed.

DD FORM 1 JAN 73 1473 EDITION OF 1 NOV 65 IS OBSOLETE
S/N 0102-014-6601

SECURITY CLASSIFICATION OF THIS PAGE (When Data Entered)

CONTENTS

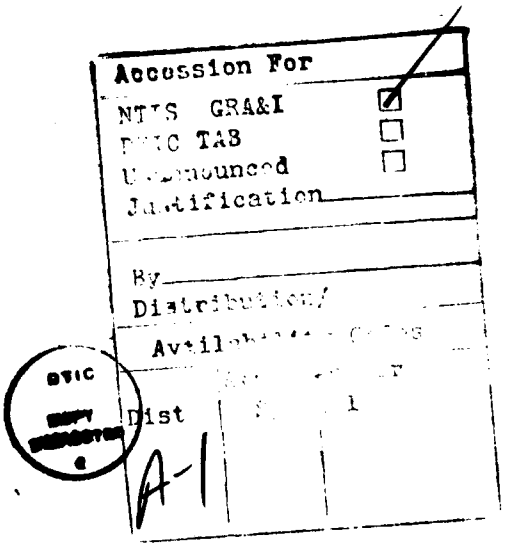

NONLINEAR MODE COUPLING THEORY OF THE LOWER-HYBRID-DRIFT INSTABILITY

I. Introduction

The lower-hybrid-drift instability has been of considerable interest to plasma physicists for more than a decade as a driving mechanism for the anomalous transport of particles, momentum and energy in both laboratory and space plasmas. In laboratory applications, this instability was initially studied to explain anomalous sheath broadening in theta pinch implosions, but has recently been applied to other laboratory confinement devices such as toroidal reversed field pinches[2] and compact torii.[3] In space plasma, it has been proposed as a mechanism to provide anomalous resistivity for reconnection events in the magnetosphere.[4] Experimentally, the lower-hybrid-drift instability has been observed in a recent theta pinch experiment,[5] and satellite data indicate that it exists in the earth's magnetotail and magnetopause.[6]

The linear theory of the lower-hybrid-drift instability is well understood.[7-9] The mode can be excited in inhomogeneous plasmas when $\rho_i/L_n > (m_e/m_i)^{1/4}$ where ρ_i is the mean ion Larmor radius and L_n is the scale length of the density gradient. At maximum growth it is characterized by $\omega_r \lesssim \omega_{lh}$, $\gamma \lesssim \omega_r$, $\underset{\sim}{k}\cdot\underset{\sim}{B} = 0$, and $k\rho_{es} \sim 1$ where $\omega = \omega_r + i\gamma$, ω_{lh} is the lower hybrid frequency and $\rho_{es} = \rho_i(m_e/2m_i)^{1/2}$. Since the instability is high frequency ($\omega >> \Omega_i$) and short wavelength ($k\rho_i >> 1$) the ions are treated as unmagnetized while the electrons are treated as strongly magnetized. In the weak drift regime $V_{di}/v_i < 1$ (where V_{di} is the ion diamagnetic drift velocity and v_i is the ion thermal velocity), $\omega \lesssim kV_{di}$ and the mode is driven unstable by the resonant interaction of the drift wave with the ions. In finite β plasmas, electrons also resonate with the wave via their ∇B drift. The resultant electron damping is stabilizing for $k\rho_{es} > 1$. In the high drift regime ($V_{di}/v_i > 1$), the mode is driven unstable via the interaction of a positive energy lower hybrid wave and a negative energy drift wave. In this paper we focus on the weak drift regime.

The nonlinear development of the lower-hybrid-drift instability is complex and not as well understood as the linear theory. A variety of nonlinear saturation mechanisms have been proposed to date. Ion trapping[10] and stochastic electron heating[11] have been proposed to quench the growth of the instability in particle simulations. However, ion trapping is not a

Manuscript approved September 7, 1983.

viable saturation mechanism when a broad 2D spectrum of waves is excited,[12] and it has not been observed in recent simulations using realistic mass ratios where such spectra develop.[13] Stochastic electron heating does not onset until a rather large threshold, $\tilde{n}/n \gtrsim 0.25$, is exceeded where $\tilde{n}$ is the density fluctuation of the wave. A wave energy bound based on the available free-energy in the relative electron-ion flow (current) has also been invoked to calculate a maximum wave amplitude.[14] In a finite β plasma, however, the current and self-consistent magnetic field are coupled and the magnetic field energy can also be tapped.[15] The free energy then becomes extremely large and does not realistically act as a bound. Finally, electron resonance broadening has been proposed as a saturation mechanism.[16] It has been recently shown in more refined calculations that "resonance broadening" does not cause a net dissipation of energy but merely leads to an exchange of energy between modes in $\underset{\sim}{k}$ space unless wave-particle resonances are included.[17,18] This mechanism can therefore only stabilize the wave spectrum in finite β plasmas.[19]

In this paper we present a nonlinear mode coupling theory of the lower-hybrid-drift instability. Our preliminary calculations have been presented previously.[20] The basic result is that the instability can saturate by transferring energy from growing, long-wavelength modes to damped, short-wavelength modes. This saturation mechanism is consistent with recent computer simulations[13] and with experimental observations.[5] In this paper, we extend the earlier theory to self-consistently incorporate finite β effects, and to include electron collisions in order to compare our results with experimental observations.

The organization of the paper is as follows. In the next section we derive the nonlinear wave equation and the wave energy transfer with the two basic nonlinearities: the nonlinear electron $\underset{\sim}{E} \times \underset{\sim}{B}$ and polarization drifts. In Section III we discuss the numerical methods used to study the mode coupling process. In Section IV we present results based upon VB electron damping of the short wavelength modes, while in Section V we present results based upon collisional damping of the modes. In Section VI we summarize our theory, compare our theoretical results with experimental observations, and discuss some applications of our results to space plasmas.

II. Derivation of the Mode Coupling Equation

We consider a slab equilibrium of cold electron and warm ions with a density profile $n_0(x)$ supported by a magnetic field $\underset{\sim}{B} = B_0(x)\hat{e}_z$ as shown in Fig. 1. Equilibrium pressure balance requires

$$\frac{\partial}{\partial x}\left[P_0(x) + B_0^2(x)/8\pi\right] = 0. \tag{1}$$

The ratio of thermal to magnetic pressure, $\beta = 8\pi n T_i/B_0^2$, is assumed to be of order unity so that electromagnetic corrections to the lower-hybrid-drift instability must be retained. The equilibrium ion velocity distribution is taken to be a Maxwellian with an average drift velocity $\underset{\sim}{V}_i = V_{di}\hat{e}_y$ where $V_{di} = (v_i^2/2\Omega_i)\partial\, \ell n\, n/\partial x$, $v_i^2 = 2T_i/m_i$ and $\Omega_i = eB_0/m_i c$.

Because of the flute nature of the instability ($\underset{\sim}{k}\cdot\underset{\sim}{B} = 0$), we self-consistently limit the spatial variations to the xy plane. In this limit the electric and magnetic fields can be represented by the scalar potential ϕ and the vector potentials A_x and A_y as[8]

$$\underset{\sim}{B} = B_z\hat{e}_z = \left(\partial A_y/\partial x - \partial A_x/\partial_y\right)\hat{e}_z \tag{2}$$

$$\underset{\sim}{E} = -\nabla\phi - c^{-1}\partial\underset{\sim}{A}/\partial t \tag{3}$$

with $\nabla\cdot\underset{\sim}{A} = 0$. Even when $\beta \sim 1$, the induction component of $\underset{\sim}{E}$ is small so that it can generally be discarded except when the $\nabla\phi$ component of $\underset{\sim}{E}$ does not contribute.

We are interested in time scales of order $\partial/\partial t >> \Omega_i$ so that the ion response to both the equilibrium and perturbed magnetic fields can be neglected. Furthermore, in the weak drift regime the ions respond to the perturbed potential ϕ adiabatically to lowest order since $\partial/\partial t << v_i|\nabla|$.[8] Thus,

$$n_i \simeq n_0\left[1 + \sqrt{\pi}\, v_i^{-1}|\nabla^{-1}|\left(\frac{\partial}{\partial t} + V_{di}\frac{\partial}{\partial y}\right)\right]\exp\left(-e\phi/T_i\right), \tag{4}$$

where the term proportional to $\sqrt{\pi}$ in (4) is a small correction describing the resonant ion interaction.

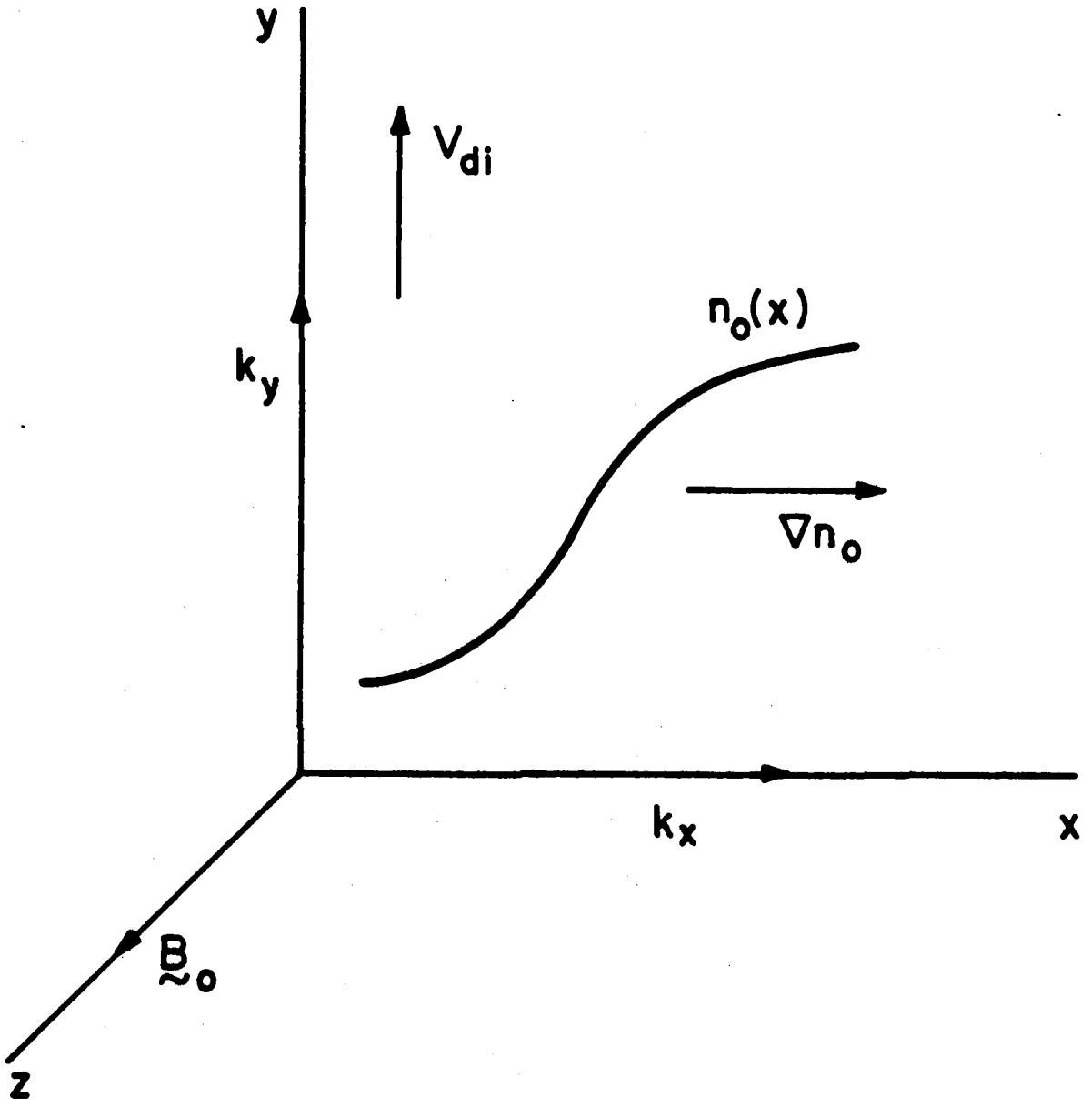

Fig. 1: The basic equilibrium configuration is shown. The unstable wave spectrum is taken to be two-dimensional with $\underset{\sim}{k} \cdot \underset{\sim}{B}_0 = 0$.

In contrast to the ions, the electrons are strongly magnetized since $\partial/\partial t \ll \Omega_e$. The electron motion is simply given by the $\underset{\sim}{E} \times \underset{\sim}{B}$ and polarization drifts,

$$\underset{\sim}{V}_e = \frac{c}{B_z} \underset{\sim}{E} \times \hat{e}_z - \frac{c}{\Omega_e} \frac{d}{dt} \frac{\underset{\sim}{E}}{B_z} \tag{5}$$

where $d/dt = \partial/\partial t + \underset{\sim}{V}_E \cdot \nabla$ and $\underset{\sim}{V}_E = c\underset{\sim}{E} \times \hat{e}_z/B_z$. The electron density can be calculated from the continuity equation,

$$d \ln n_e/dt + \nabla \cdot \underset{\sim}{V}_e = 0. \tag{6}$$

The electron compression $\nabla \cdot \underset{\sim}{V}_e$ is obtained from Eq. (5). To lowest order,

$$\nabla \cdot \underset{\sim}{V}_e = \frac{c}{B_z \Omega_e} \frac{d}{dt} \nabla^2 \phi - \frac{d}{dt} \ln B_z. \tag{7}$$

The first term in Eq. (7) arises from the polarization drift and the second from the compression of the flux tube in a finite β plasma. The continuity equation can now be written as

$$\frac{d}{dt} \ln(n_e/B_z) + \frac{c}{B_z \Omega_e} \frac{d}{dt} \nabla^2 \phi = 0 \tag{8}$$

so that the rate of change of the number of electrons in a flux tube (n_e/B_z) is given by the polarization drift. The time variation of B_z in Eq. (8) is calculated from Ampere's Law

$$\nabla^2 A_x = -(4\pi/c) J_x = -(4\pi n_e/B_z) \partial\phi/\partial y, \tag{9}$$

where J_x is dominated by the $\underset{\sim}{E} \times \underset{\sim}{B}$ drift of the electrons. Using $\nabla \cdot \underset{\sim}{A} = 0$, we find that $\nabla^2 A_x = -\partial B_z/\partial y$ so that

$$\frac{\partial}{\partial y} \left[\frac{B_z^2}{8\pi} - n_0 e\phi\right] = 0, \tag{10}$$

which can be integrated to evaluate

$$\frac{\partial}{\partial t} \ln B_z = \frac{\beta}{2} \frac{\partial}{\partial t} \left(\frac{e\phi}{T_i}\right) \tag{11}$$

in Eq. (7). The convective derivative of B_z can similarly be evaluated using Eq. (10) in conjunction with the equilibrium pressure balance relation,

$$\underset{\sim}{V}_E \cdot \nabla \ln B_z = \frac{\beta}{2} \frac{c}{B_z} \frac{\partial \ln n}{\partial x} \frac{\partial \phi}{\partial y} . \tag{12}$$

Finally, invoking charge neutrality ($n_e = n_i$) and combining (8), (11) and (12), we obtain the nonlinear equation

$$\begin{aligned} &(1 - \hat{\nabla}^2)\hat{\phi}_\tau + \hat{\phi}_y - \gamma_0 |\hat{\nabla}^{-1}|(\hat{\phi}_{\tau\tau} + \hat{\phi}_{\tau y}) + \gamma_e \hat{\phi} \\ &+ (\hat{\nabla}\hat{\phi} \times \hat{e}_z \cdot \hat{\nabla})\hat{\nabla}^2\hat{\phi} + \gamma_0 \hat{\nabla}\hat{\phi} \times \hat{e}_z \cdot \hat{\nabla} |\hat{\nabla}^{-1}|(\hat{\phi}_\tau + \hat{\phi}_y) = 0 \end{aligned} \tag{13}$$

where

$$\hat{\nabla} = \frac{\rho_{es}}{(1+\beta/2)^{1/2}} \nabla$$

$$\tau = \frac{\rho_{es}}{L_n} \Omega_e (1 + \beta/2)^{1/2} t$$

$$\hat{\phi} = \frac{L_n}{\rho_{es}} (1 + \beta/2)^{1/2} \frac{e\phi}{T_i}$$

$$\gamma_0 = \pi^{1/2} (V_{di}/v_i)/(1 + \beta/2)$$

and the subscripts on $\hat{\phi}$ denote a derivative with respect to that variable. The quantity γ_e represents the wave damping due to electrons, which can result either from ∇B resonant particles in a finite β plasma[8] or collisional viscosity.[21] Equation (13) is only valid for $\gamma_0 < 1$ since the adiabatic ion response can only be justified in this limit. Linearizing this equation, we obtain the complex eigenvalue (in our normalized units),

$$\hat{\omega} = \hat{\omega}_k = \frac{\hat{k}_y}{1+\hat{k}^2} + i\gamma_0 \frac{|\hat{k}|\, \hat{k}_y^2}{(1+\hat{k}^2)^3} - i \frac{\gamma_e}{1+\hat{k}^2} . \tag{14}$$

Since Eq. (13) is second order in time, there is an additional root,

$$\hat{\omega} = i|\hat{k}|(1 + \hat{k}^2)/\gamma_0, \tag{15}$$

which is spurious since it violates the assumption that $\hat{\omega} \ll kv_i$. This root is growing and therefore must be eliminated before carrying out our numerical computations (see Sec. III).

In the flute limit considered here, the magnetic perturbations and equilibrium VB_z do not structurally alter the equation for $\hat{\phi}$. They enter the equations through the factors $(1 + \beta/2)$ which appear in the normalized variables defined in Eq. (13). We ignore this trivial finite β modification to the equations in the remainder of this paper.

In the limit $\gamma_e, \gamma_0 \to 0$, Eq. (13) reduces to the Hasegawa-Mima equation in which the nonlinearity arises from the nonlinear polarization drift.[22] This equation has two invariants, energy and enstrophy, neither of which is preserved in the more general Eq. (13). When γ_0 is finite, the $\underset{\sim}{E} \times \underset{\sim}{B}$ nonlinearity also appears in Eq. (13). This nonlinearity has been considered previously in studies of universal mode turbulence.[23,24]

Our calculation differs from previous work in that we do not make the quasi-linear hypothesis that

$$\hat{\phi}_\tau + \hat{\phi}_y \approx -i(\hat{\omega}_k - \hat{k}_y)\hat{\phi} \tag{16}$$

in the terms proportional to γ_0 in Eq. (13). Thus, our equation is second order in time rather than first order. In Sec. III it is shown that the spectrum always saturates when $\hat{\phi} \sim 1$ so that the linear and nonlinear terms in Eq. (13) are comparable. The quasi-linear hypothesis can therefore not be justified in drift-wave turbulence. A similar second order equation has been derived for dissipative drift waves.[26]

It is recognized that both universal and dissipative drift wave turbulence are inherently three-dimensional since $k_\parallel = \underset{\sim}{k}\cdot\underset{\sim}{B}/B$ is required for the mode to exist and the spatial variations in the two directions perpendicular to $\underset{\sim}{B}$ are required to calculate the mode coupling. In 2-D models of this turbulence the coupling of modes with differing $k_\parallel$'s is ignored.[23-26] There is no theoretical justification for this procedure so that care must be taken in applying the results of model calculations to experimental observations. By contrast, the lower-hybrid-drift instability

is a flute mode so that the neglect of the coupling along $\underset{\sim}{B}$ can be justified and the results of the 2-D model can be directly compared with experimental observations.

A qualitative understanding of the direction of the flow of energy described by Eq. (13) can be obtained by calculating the stability of a single, large-amplitude wave $\hat{\phi}_0$ with $\hat{k}_0$ and $\hat{\omega}_0$ satisfying the linear dispersion relation in Eq. (14). A perturbation of wavevector $\underset{\sim}{k}$ is coupled through the pump to modes with $\hat{\underset{\sim}{k}} \pm p\,\hat{\underset{\sim}{k}}_0$ ($p = 1,2,\ldots$). For simplicity, we consider only the coupling of $(\hat{\omega}, \hat{\underset{\sim}{k}})$ with its nearest neighbors $(\hat{\omega}_\pm, \hat{\underset{\sim}{k}}_\pm)$ where $\hat{\omega}_\pm = \hat{\omega} \pm \hat{\omega}_0$ and $\hat{\underset{\sim}{k}}_\pm = \hat{\underset{\sim}{k}} \pm \hat{\underset{\sim}{k}}_0$, i.e., $p = 1$. The dispersion relation for this $(\hat{\underset{\sim}{k}}, \hat{\underset{\sim}{k}}_\pm)$ coupled system is (see Appendix)

$$\varepsilon(\hat{\omega}, \hat{\underset{\sim}{k}}) + |\hat{\phi}_0|^2\left[\frac{M(-\hat{\underset{\sim}{k}}_0, \hat{\underset{\sim}{k}}_+)M(\hat{\underset{\sim}{k}}, \hat{\underset{\sim}{k}}_0)}{\varepsilon(\hat{\omega}_+, \hat{\underset{\sim}{k}}_+)} + \hat{k}_0 + -\hat{k}_0\right] = 0 \tag{17}$$

where

$$\varepsilon(\hat{\omega}, \hat{\underset{\sim}{k}}) = \hat{\omega}\left[1 + \hat{k}^2(1 - i\delta_k)\right] - \hat{k}_y + i\gamma_e$$

$$\delta_k = \gamma_0(\hat{k}_y - \hat{\omega})/\hat{k}^3$$

$$M(\hat{\underset{\sim}{k}}_1, \hat{\underset{\sim}{k}}_2) = \hat{\underset{\sim}{k}}_1 \times \hat{\underset{\sim}{k}}_2 \cdot \hat{e}_z\left[\hat{k}_1^2(1 - i\delta_{k1}) - \hat{k}_2^2(1 - i\delta_{k2})\right]$$

When γ_0 and γ_e are neglected in Eq. (17) and we take the limit $\hat{\omega} \gg \hat{\omega}_k$, the dispersion relation simplifies to

$$\hat{\omega}^2 = |\hat{\phi}_0|^2(\hat{\underset{\sim}{k}}_0 \times \hat{\underset{\sim}{k}} \cdot \hat{e}_z)^2 \frac{\hat{k}_0^2 - \hat{k}^2}{1+\hat{k}^2}\left(\frac{\hat{k}_0^2 - \hat{k}_+^2}{1+\hat{k}_+^2} + \frac{\hat{k}_0^2 - \hat{k}_-^2}{1+\hat{k}_-^2}\right). \tag{18}$$

The decay modes are purely growing with a growth rate which peaks around $\hat{\underset{\sim}{k}} \cdot \hat{\underset{\sim}{k}}_0 = 0$ with $\hat{k}/\hat{k}_0 \approx 0.6 - 0.8$, depending on the magnitude of $\hat{k}_0$. A necessary requirement for instability is that one of the three decay modes $(\hat{\underset{\sim}{k}}, \hat{\underset{\sim}{k}}_\pm)$ has a longer wavelength than the pump.[27] This decay process with $\hat{\underset{\sim}{k}} \cdot \hat{\underset{\sim}{k}}_0 = 0$ and $\hat{k}/\hat{k}_0 \lesssim 1$ is clearly seen in our numerical simulation during the initial phase of saturation (Sec. III) of the instability. For this situation, in which Eq. (13) reduces to the Hasegawa-Mima equation, the wave energy inevitably cascades to longer and longer wavelengths so that no stationary wave spectrum can result.[28]

When γ_0 is included, this conclusion no longer remains valid. Taking the limit $\hat{k}_0 << \hat{k}$ and again assuming $\hat{\omega} >> \hat{\omega}_k$, the dispersion relation is given by

$$\hat{\omega}^2 = \frac{2|\hat{\phi}_0|^2|\hat{\underset{\sim}{k}} \times \hat{\underset{\sim}{k}}_0 \cdot \hat{e}_z|^2\hat{k}^4}{1+\hat{k}^2}\left[1 + i\,\frac{\gamma_0\hat{\omega}(2+\hat{k}^2)}{\hat{k}^3(1+\hat{k}^2)}\right] . \tag{19}$$

Equation (19) yields a dissipative instability when γ_0 is finite. The destabilizing term can be traced back to the $\underset{\sim}{E} \times \underset{\sim}{B}$ nonlinearity. This dissipative instability produces a flow of energy from long to short wavelength and, as will be demonstrated, prevents the condensation of wave energy at long wavelengths, enabling the wave spectrum to reach a steady state.

The dispersion relation in Eq. (19) contains no amplitude threshold for instability as long as $\underset{\sim}{k}$ is in the proper direction. In the more general dispersion relation in Eq. (17), where the linear frequencies are retained, $\hat{\phi}_0$ must exceed a threshold before the instability onsets unless the frequency matching condition

$$\Delta\hat{\omega} \equiv \hat{\omega}_k - \hat{\omega}_{k\pm} \pm \hat{\omega}_0 = 0 \tag{20}$$

is satisfied. For $\hat{\underset{\sim}{k}}_0 = \hat{k}_0\hat{e}_y$ and $\hat{k}_0$, $\hat{k} << 1$, this matching condition becomes

$$\hat{k}_x^2 = -\,3(\hat{k}_y^2 + \hat{k}_y\hat{k}_0). \tag{21}$$

The locus of modes which satisfies Eq. (20), those with $\hat{k}_y < 0$ and $|\hat{k}_y| < \hat{k}_0$, are shown in Fig. 2. There is no threshold for instability of these modes (neglecting dissipation). Nevertheless, for the lower hybrid drift instability both of the decay modes $\underset{\sim}{k}$ and $\underset{\sim}{k} + \underset{\sim}{k}_0$ shown in Fig. 2 are individually unstable so that the mode coupling process can not saturate the instability.

Interacting modes with $\Delta\hat{\omega} \neq 0$ can be driven unstable when $\hat{\phi}_0$ exceeds a threshold. For the case $\hat{\underset{\sim}{k}}_0 = \hat{k}_0\,\hat{e}_y$, this threshold can be easily calculated. The dispersion relation in Eq. (17) simplifies to

$$\hat{\omega}^2 = (\hat{\omega}_0 - \hat{\omega}_{k+})^2 - 2\,\frac{|\hat{\phi}_0|^2\hat{k}^4\hat{k}_0^2(\hat{k}_0^2 - \hat{k}^2)}{(1+\hat{k}^2)(1+\hat{k}^2{}_0+\hat{k}^2)}, \tag{22}$$

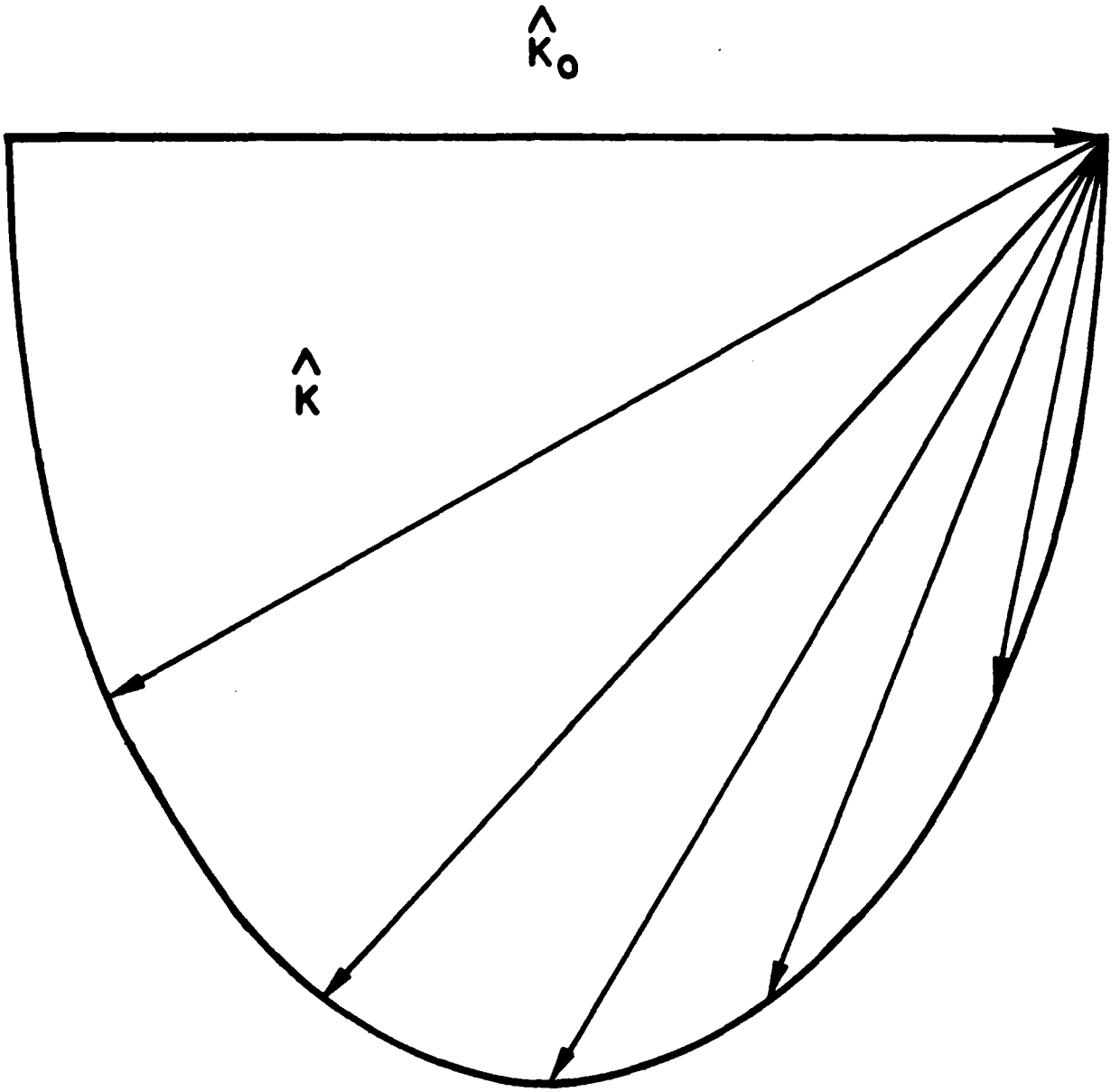

Fig. 2: The locus of modes $\hat{k}_x = k\rho_{e,s}$ which satisfy the frequency matching condition $\Delta\hat{\omega} = \hat{\omega}_k - \omega_{k\pm} \pm \omega_0 = 0$, with $k_{\pm} = k \pm k_0$ and $\hat{\omega}_k = \hat{k}_y/(1 + \hat{k}^2)$, is shown.

where the dissipative sources and sinks have been neglected. In this limit $\hat{\omega}_k \propto \hat{k}_y = 0$ and $\omega_{k+} = -\omega_{k-}$ so that $\Delta\hat{\omega} = \hat{\omega}_0 - \hat{\omega}_{k+}$ is the frequency mismatch. To have instability,

$$|\hat{\phi}|^2 > |\hat{\phi}_0|_c^2 \equiv \frac{1 + \hat{k}^2}{2(1 + \hat{k}^2 + \hat{k}_0^2)(1 + \hat{k}_0^2)(\hat{k}_0^2 - \hat{k}^2)} . \tag{23}$$

For cases of interest $\hat{k}_0 \sim 1$ and $|\hat{\phi}_0|_c \approx .25$. At this amplitude the nonlinearity overcomes the linear frequency mismatch of the modes and a broad range of modes is driven unstable. As a consequence, we would expect the wave spectrum to saturate at around this level even when $\gamma_0 \ll 1$, i.e., the driving rate is small. This conclusion is verified in our numerical computations.

The particle flux can be calculated self-consistently with the wave spectrum. The rate of change of the density $\bar{n}(x) \equiv \langle n_e(x,y)\rangle_y$, where $\langle\ \rangle_y$ is a spatial average over y, is obtained by averaging the electron continuity equation,

$$\frac{\partial \bar{n}}{\partial t} + \frac{\partial}{\partial x}\langle n_e V_{ex}\rangle_y = 0. \tag{24}$$

To lowest order, $V_{ex} \approx -(c/B)\partial\phi/\partial y$, the polarization drift being small. The electron density can not be calculated directly since Eq. (24) for n_e can not be inverted analytically. However, since $n_e \approx n_i$, we can use the expression for n_i in Eq. (4) to obtain an explicit expression for the diffusion coefficient $D = -\langle n_e V_{ex}\rangle_y / (\partial\bar{n}/\partial x)$,

$$\hat{D} = D/D_0 = \left(\frac{2}{\pi}\right)^{1/2} \gamma_0^2 \sum_k \frac{\hat{k}_y}{|\hat{k}|} \hat{\phi}_k\left(\hat{k}_y\hat{\phi}_k - i\frac{\partial\hat{\phi}_k}{\partial\tau}\right). \tag{25}$$

$$D_0 = \rho_{es}^2\omega_{1h}$$

Note that the normalization factor D_0 of the diffusion coefficient corresponds to a step size ρ_{es} with a correlation time ω_{1h}^{-1}. In the quasilinear limit $\partial/\partial\tau = -i\hat{\omega}_k$ and $\hat{D}$ is given by

$$\hat{D}_{ql} = \left(\frac{2}{\pi}\right)^{1/2} \gamma_0^2 \sum_k \hat{k}\,\hat{k}_y^2 |\hat{\phi}_k|^2 (1 + \hat{k}^2)^{-1}. \tag{26}$$

The time evolution of both $\hat{D}$ and $\hat{D}_{ql}$ will be computed along with the wave spectrum in Sec. III.

III. Numerical Computations

The nonlinear equation for $\hat{\phi}$ in Eq. (13) is too complex to solve analytically and we have therefore adopted a computational approach. It is convenient to separate the second order Eq. (13) into two complex first order equations by defining a new function

$$\psi \equiv \hat{\nabla}^2\hat{\phi} + \gamma_0|\hat{\nabla}^{-1}|(\hat{\phi}_\tau + \hat{\phi}_y). \tag{27}$$

Equation (13) for $\hat{\phi}$ can then be written as

$$\hat{\phi}_\tau - \psi_\tau + \hat{\phi}_y + \gamma_e\phi + \hat{\nabla}\hat{\phi} \times \hat{e}_z\cdot\hat{\nabla}\psi = 0. \tag{28}$$

Since $\gamma_0 \ll 1$, we find from Eq. (27) that to lowest order

$$\hat{\phi} \simeq \hat{\nabla}^{-2}\psi. \tag{29}$$

The second term on the right side of Eq. (27) is already small since it is proportional to γ_0 so that $\hat{\phi}$ in this term can be approximated to lowest order. Equation (27) then becomes an evolution equation for ψ,

$$\psi_\tau = -\psi_y + |\hat{\nabla}|\hat{\nabla}^2(\psi - \hat{\nabla}^2\hat{\phi})/\gamma_0. \tag{30}$$

Finally, eliminating ψ_τ in Eq. (28) using Eq. (30), we obtain a similar evolution equation for $\hat{\phi}$,

$$\hat{\phi}_\tau = -\hat{\phi}_y + \gamma_e\hat{\phi} - \psi_y + |\hat{\nabla}|\hat{\nabla}^2(\psi - \hat{\nabla}^2\hat{\phi})/\gamma_0 - \hat{\nabla}\hat{\phi} \times \hat{e}_z\cdot\hat{\nabla}\psi. \tag{31}$$

Note that the iteration procedure which was carried out on Eq. (27) eliminated the spurious unstable root. The dispersion relation which results from linearizing Eqs. (30) and (31) yields the correct eigenvalue of the lower hybrid drift instability given in Eq. (14) plus a spurious damped root,

$$\hat{\omega} = -i|\hat{k}|^3(1 + \hat{k}^2)/\gamma_0, \tag{32}$$

which does not cause any numerical difficulties. All of our numerical computations are based on the two coupled equations for $\hat{\phi}$ and ψ in (30) and (31).

The inclusion of the electron damping $\hat{\gamma}_e$ in Eq. (31) is essential in order to obtain a saturated spectrum since in the absence of this term all modes in $\underset{\sim}{k}$ space are unstable [see the growth rate in Eq. (14)]. We have used two forms of electron dissipation in our calculations. The first arises from the VB resonant electrons in a finite β plasma. Explicit expressions for this damping rate have been derived in Ref. 9. In the long wavelength limit

$$\gamma_e = \gamma_{e0}|\hat{k}_y|\hat{k}^4 \tag{33}$$

with

$$\gamma_{e0} = \pi \frac{(1 + 2\beta_i)^2}{\beta_i \beta_e^2 (2 + \beta_i)} \exp(-2/\beta_e) \tag{34}$$

where β_e and β_i are the individual electron and ion values of beta. In the short wavelength limit, $\hat{\gamma}_e$ scales as $\hat{k}_y\hat{k}^2$ so we take as a model

$$\gamma_e = \gamma_{e0}\hat{k}_y\hat{k}^4/(1 + \hat{k}^2). \tag{35}$$

An important feature of the VB resonant damping is that it scales as $\hat{k}^5$ as $\hat{k} \to 0$. Since the growth term in Eq. (14) scales as $\hat{k}^3$ in the long wavelength limit, modes with $\hat{k}_x = 0$ remain unstable even as $\hat{k}_y \to 0$. For large $\hat{k}$ all modes are stable. The boundary between stable and unstable regions of $\underset{\sim}{k}$ space is shown in Fig. 3a for $\gamma_{e0}/\gamma_0 = 0.1$ and 1.0. The area below the bounding curves is unstable. As γ_{e0}/γ_0 increases the unstable spectrum collapses toward long wavelength but unstable modes always remain.

Electron collisional viscosity is important in laboratory experiments where measurements of lower-hybrid-drift wave turbulence have been made. The electron damping rate for this case is given by[21]

$$\gamma_e = \nu_0 \hat{k}^2 \tag{36}$$

where

$$\nu_0 = \nu_e L_n / \Omega_e \rho_{es}, \tag{37}$$

ν_e is the electron-ion collision frequency

$$\nu_e = 2.9 \times 10^{-6} (\lambda n_e / T_e^{3/2}) s^{-1},$$

λ is the Coulomb logarithm, n_e is the electron density in cm^{-3} and T_e is the electron temperature in ev. In this case the collisional damping dominates the growth at both large and small $\hat{k}$ so that the unstable region of $\hat{k}$ space is localized around $\hat{k} \sim 1$ as shown in Fig. 3b for several values of ν_0/γ_0. There is no instability when $\nu_0/\gamma_0 > \sqrt{3}/16$.

The coupled equations for $\hat{\phi}$ and ψ in (30) and (31) are solved using a pseudo-spectral method code developed by Fyfe et al.,[29] based on the work of Orszag.[30] The dependent variables $\hat{\phi}$ and ψ are Fourier-decomposed,

$$\hat{\phi}(\hat{x},\tau) = \sum_{\hat{k}} \hat{\phi}(\hat{k},\tau) \exp(i\hat{k}\cdot\hat{x}), \tag{38}$$

where $\hat{k} = n/\lambda$ and $n = n_x \hat{e}_x + n_y \hat{e}_y$ with n_x and n_y integers. The parameter λ fixes the value of $|n|$ for which $|\hat{k}| = 1$. The nonlinear term in Eq. (31) is computed by fast Fourier transforming $\hat{\nabla}\hat{\phi}$ and $\hat{\nabla}\psi$ from $\hat{k}$ to configuration space, calculating the product $\hat{\nabla}\hat{\phi} \times \hat{e}_z \cdot \hat{\nabla}\psi$ in configuration space and then fast Fourier transforming the result back to $\hat{k}$ space. The equations are then stepped forward in time in $\hat{k}$ space and the cycle is repeated.

The numerical results presented in this paper are nominally computed on a 32 x 32 mesh. However, to prevent aliasing of the wave energy during the fast Fourier transformation, it is necessary to zero all modes with $n > 32/3$ so that the useful volume of k space is actually much less than one would expect.

A number of tests have been made to ensure that the code is correctly advancing the equations in time. The growth rates of the modes as obtained from the code during the linear growth phase have been checked with the

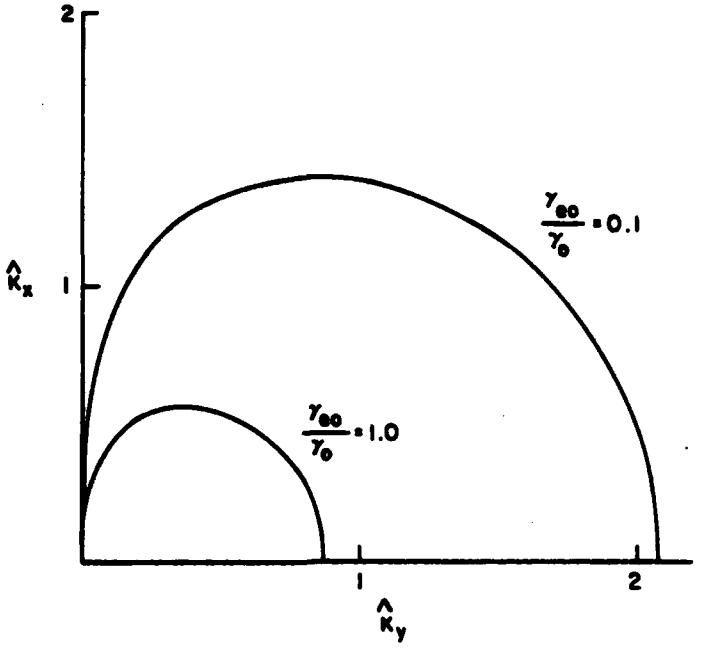

(a)

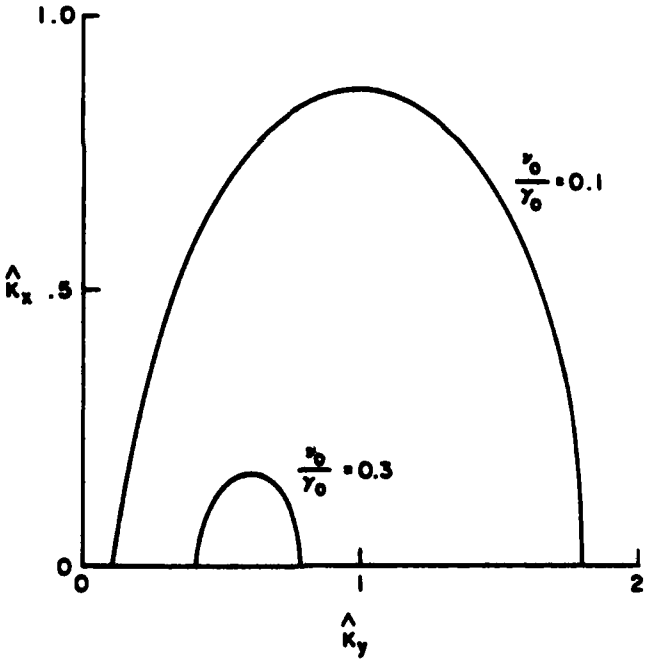

(b)

Fig. 3: The region of instability in $\hat{k}$ space (below bounding curves) is shown for (a) collisionless plasma and (b) collisional plasma, where γ_0, γ_{e0} and ν_0 are the normalized ion growth rate, electron VB damping rate and electron collisional damping rate. Collisional damping stabilizes the spectrum for $\gamma_{e0}/\gamma_0 > \sqrt{3}/16$.

solution of the linear dispersion relation. We have zeroed all but three interacting modes in the full code and cross-checked their nonlinear behavior with an independent code written to specifically study the interaction of only three waves. The sensitivity of our results to the step size of the time integration, as well as to the number of modes (some runs have been carried out on a 64 x 64 mesh), have also been checked.

IV. Numerical Results: Collisionless Damping

In collisionless, finite-β plasmas the VB resonant electron damping limits the range of unstable modes as shown in Fig. 3a. In this section we present the results of our numerical computations for this case. Preliminary results were previously presented for this collisionless case although the structure of our electron damping is now more realistic than that which was used in past computations.[20]

In Figs. 4-6 we present in some detail the results of our computations for the case $\gamma_0 = 0.5$, $\gamma_{e0} = 0.01$ and $\lambda = 5$ ($k_y \rho_{es} = 1$ for $n_y = 5$). The $\hat{\phi}$ spectrum is initialized with random noise with $\phi \sim 10^{-3}$ and Eqs. (30) and (31) are evolved until the wave energy (in our normalized units),

$$\hat{W} = \frac{1}{2} \sum_k (1 + \hat{k}^2) |\hat{\phi}_k|^2, \tag{39}$$

approaches a steady state value. The time history of $\hat{W}$, the root-mean-square potential,

$$\hat{P} = \langle \hat{\phi}^2 \rangle^{1/2} \equiv \left(\sum_k |\hat{\phi}_k|^2 \right)^{1/2} \tag{40}$$

and the diffusion coefficients $\hat{D}$ and $\hat{D}_{ql}$ [Eqs. (25) and (26), respectively] are shown in Fig. 4. All of these quantities exhibit a similar temporal behavior. The initial decay ($\tau < 4$) is associated with the rapid dissipation of energy initialized in the damped modes, and is followed by a linear growth phase ($4 < \tau < 30$). Subsequently, mode coupling occurs which leads to saturation of the instability, albeit with some initial overshoot ($\tau \sim 30$). The levels of the total wave energy and other parameters of Fig. 4 are quite stationary in time after saturation. Also, the stationary values of all four quantities are relatively insensitive to the initialization of $\hat{\phi}$.

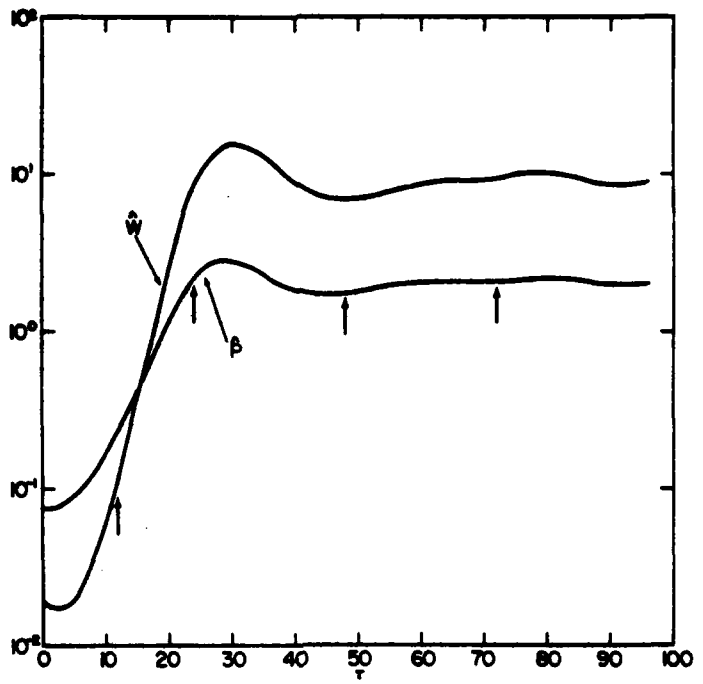

(a)

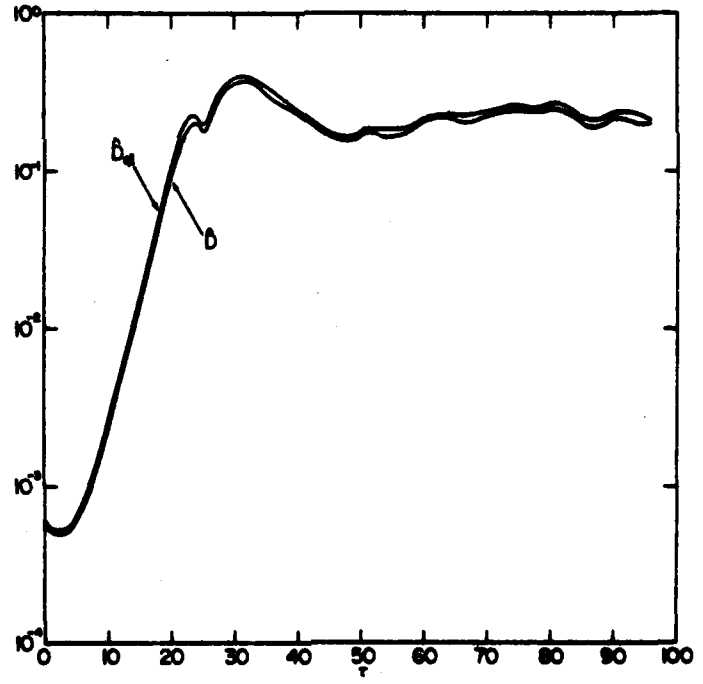

(b)

Fig. 4: The time history of the normalized wave energy $\hat{W}$, root-mean-square potential $\hat{P}$, diffusion coefficient $\hat{D}$ and quasilinear diffusion coefficient $\hat{D}_{ql}$ are shown for $\gamma_0 = 0.5$, $\gamma_{e0} = 0.01$ and $\nu_e = 0$.

In Fig. 4 the potential $\hat{P}$ asymptotes to 2.0 after saturation so that $\hat{\phi} \sim 1$, which is consistent with the discussion in Sec. II. The quasilinear diffusion coefficient ($\hat{D}_{ql}$) tracks the actual diffusion coefficient ($\hat{D}$) quite well during the entire time evolution of the instability. An important point which must be emphasized with regard to $\hat{D}$ is that both species, electrons and ions, continue to exchange both energy and momentum even after a steady state is reached; the electrons through the VB resonance and the ions by direct resonant interaction. If the instability had saturated by ion trapping and the electrons had no resonant interaction with the wave, there would be no diffusion in the steady state since the electrons could not exchange momentum with the ions. Both species must have a dissipative interaction with the waves to have diffusion.

In Fig. 5 we show a sequence of snapshots of the 2-D wave spectrum in $\underset{\sim}{n}$ space as the instability grows and saturates. The times at which the snapshots are taken are indicated by the arrows in Fig. 4a. Only $n_x > 0$ is shown since the spectrum for $n_x < 0$ can be obtained from $n_x > 0$ by the reality condition $\hat{\phi}(-\underset{\sim}{n}) = \hat{\phi}(\underset{\sim}{n})$. Figure 5a shows the spectrum during the linear phase of the instability. The spectrum is strongly peaked around the most unstable modes, $(n_x, n_y) = (0, \pm 5)$. Figure 5b shows the spectrum just prior to saturation. Note the development of the prominent peak at (4, 0), which is a marginally stable mode since $n_y = 0$, and the broadening of the main peaks of the spectrum in the n_x direction. These results are entirely consistent with the discussion of the parametric excitation of daughter waves by a pump in Sec. II. The pump wave $(0, \pm 5)$ couples and destabilizes the (4, 0) and $(4, \pm 5)$ modes. These secondary peaks quickly grow to large amplitude and excite other modes in turn. This mode coupling process culminates as the total wave energy saturates and spreads through most of the unstable or weakly damped volume of $\underset{\sim}{n}$ space as shown in Fig. 5c. Two significant features of Fig. 5c are: the shift in the peaks of the wave spectrum toward long wavelength $(0, \pm 2)$; and the nearly isotropic spectrum of waves surrounding these peaks. The detailed wave spectrum exhibits substantial variability in time, even after saturation when the total wave energy is nearly constant. This can be clearly seen by comparing the spectrum in Fig. 5c with that at a later time in Fig. 5d. The unstable and stable modes clearly continue to exchange energy in a dynamic manner even after saturation. Nevertheless, the wave spectra at

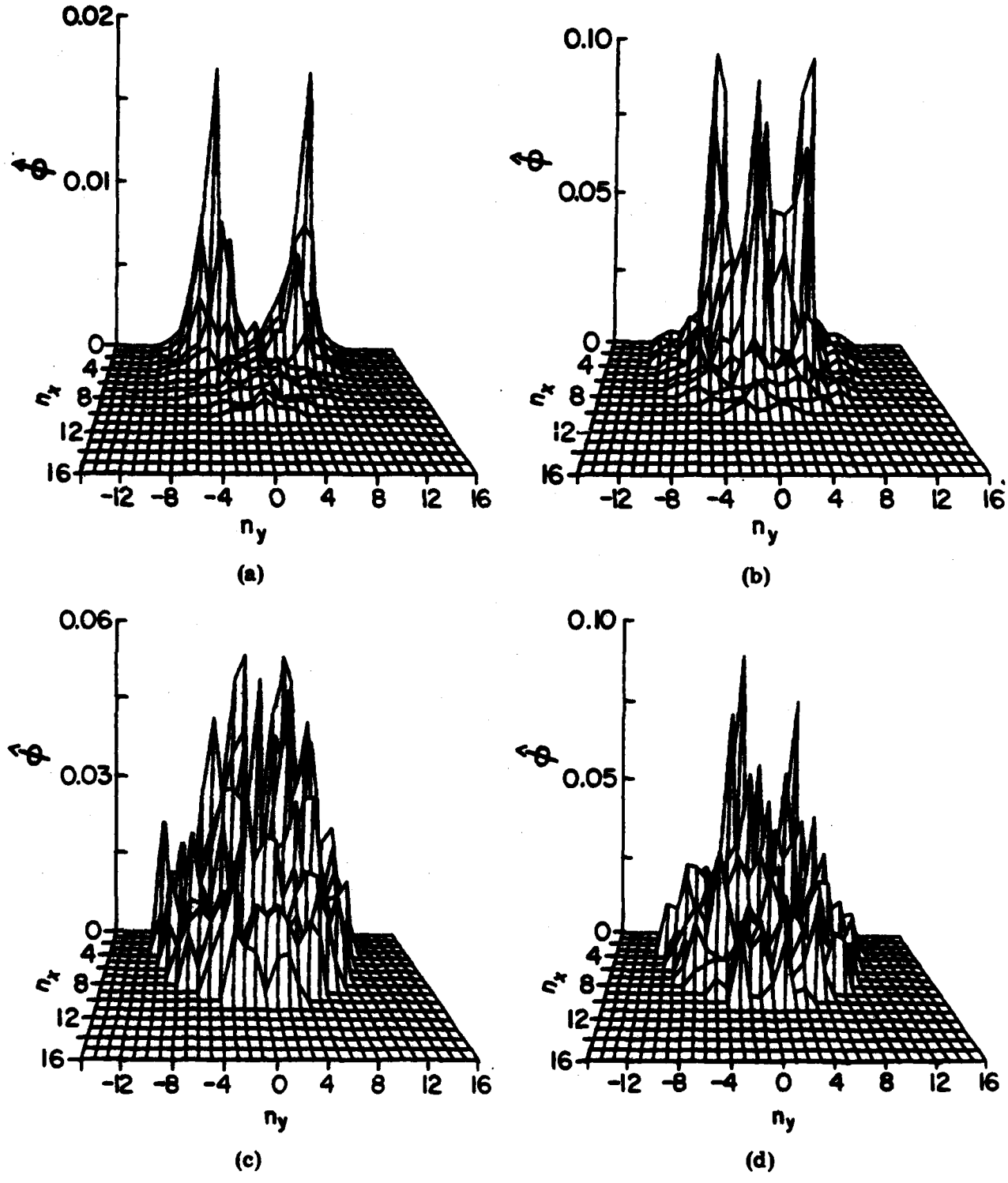

Fig. 5: Snapshots of the two-dimensional wave spectra are shown (a) during the linear phase, (b) during saturation, (c) just after saturation and (d) well after saturation for the run shown in Fig. 4, where $\underset{\sim}{n} = 5\,\hat{\underset{\sim}{k}}$. The times of the snapshots are marked with arrows in Fig. 4a.

late time are always characterized by peaks which are shifted towards long wavelength from the most unstable mode and by a broad spectrum of noise. Finally, in Fig. 6a we show the wave spectrum averaged over the time interval $112 < \tau < 192$. Much of the irregularity which was evident in the instantaneous spectra has now disappeared. The averaged spectrum is strongly peaked around $(0, \pm 3)$ with much smaller secondary peaks at $(\pm 2, 0)$. A contour plot of this average spectrum is shown in Fig. 6b. Note the cleft in the spectrum along $k_y = 0$.

A number of runs have been made with different values of the drift parameter γ_0 and the coefficient of the electron damping γ_{e0}. In Fig. 7 we show the diffusion coefficient $\hat{D}$ and potential $\hat{P}$ at saturation as functions of the drift parameter γ_0. The electron damping γ_{e0} was varied with γ_0 so that the spectrum of unstable waves in $\hat{k}$ space did not change, i.e., $\gamma_{e0} \simeq 0.1\ \gamma_0$. The potential $\hat{P}$ is quite insensitive to γ_0 while the diffusion coefficient scales approximately as γ_0^2 (the reference curve $\hat{D} = 0.76\ \gamma_0^2$ is shown for comparison). The insensitivity of $\hat{P}$, and consequently $\hat{\phi}$, to γ_0 is consistent with the idea, expressed previously in Sec. II, that the non-linear polarization drift in Eq. (13) must exceed the linear frequency mismatch of the interacting waves in order for effective energy exchange (and therefore saturation of the instability) to take place.

In Fig. 8 we show $\hat{P}$ and $\hat{D}$ as a function of γ_0 with $\gamma_{e0} = 0.11$. In this case the linearly unstable spectrum collapses towards longer wavelengths as γ_0 decreases as previously shown in Fig. 3a. The dependence of $\hat{P}$ and $\hat{D}$ on γ_0 in this case is basically similar to that in Fig. 7. The normalized potential $\hat{P}$ has a weak dependence on γ_0, increasing slightly as γ_0 decreases. The diffusion coefficient again scales as γ_0^2 (the reference curve $\hat{D} = 0.76\ \gamma_0^2$ is shown).

The somewhat surprising conclusion which can be drawn from Figs. 7 and 8 is that the diffusion coefficient $\hat{D}$ is very insensitive to the dissipation rate γ_{e0}; much less sensitive, for example, than $\hat{P}$. For $\gamma_0 = 0.25$, the diffusion coefficient $\hat{D} = 0.06$ in both Figs. 7 and 8 even though $\gamma_{e0} = 0.03$ and 0.11, respectively. By contrast, $\hat{P}$ is 50% higher in Fig. 8 than in Fig. 7 for $\gamma_0 = .25$. As γ_{e0} is increased for a fixed value of γ_0, $\hat{\phi}$ increases while the spectrum shifts towards longer wavelength so that $\hat{D}$ does not change [see Eq. (26) for $\hat{D}_{q1}$]. The shift towards long wavelength

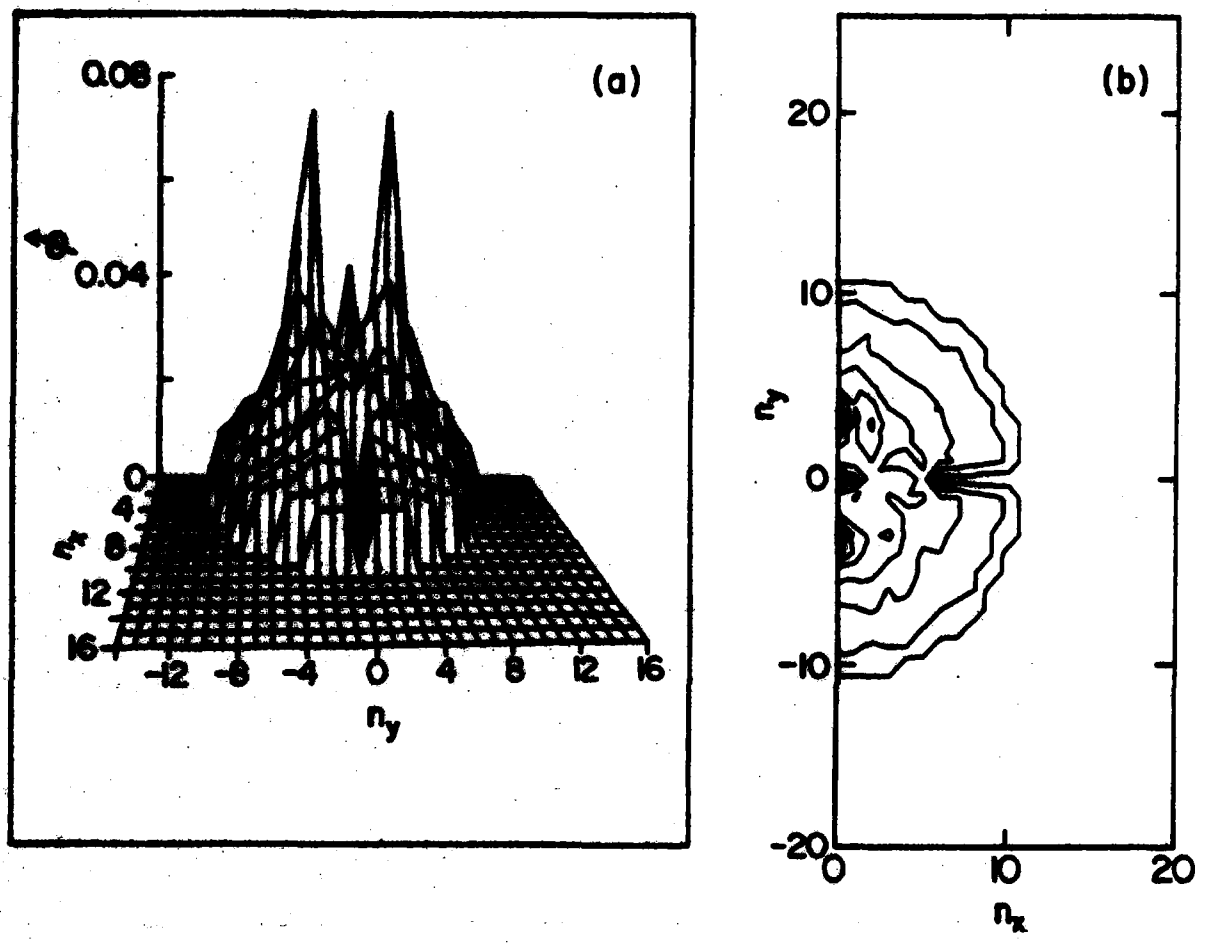

Fig. 6: The time averaged wave spectrum (a) and associated constant $\hat{\phi}$ contours (b) are shown for the run presented in Fig. 4. The spectrum was averaged over the interval $112 < \tau < 192$.

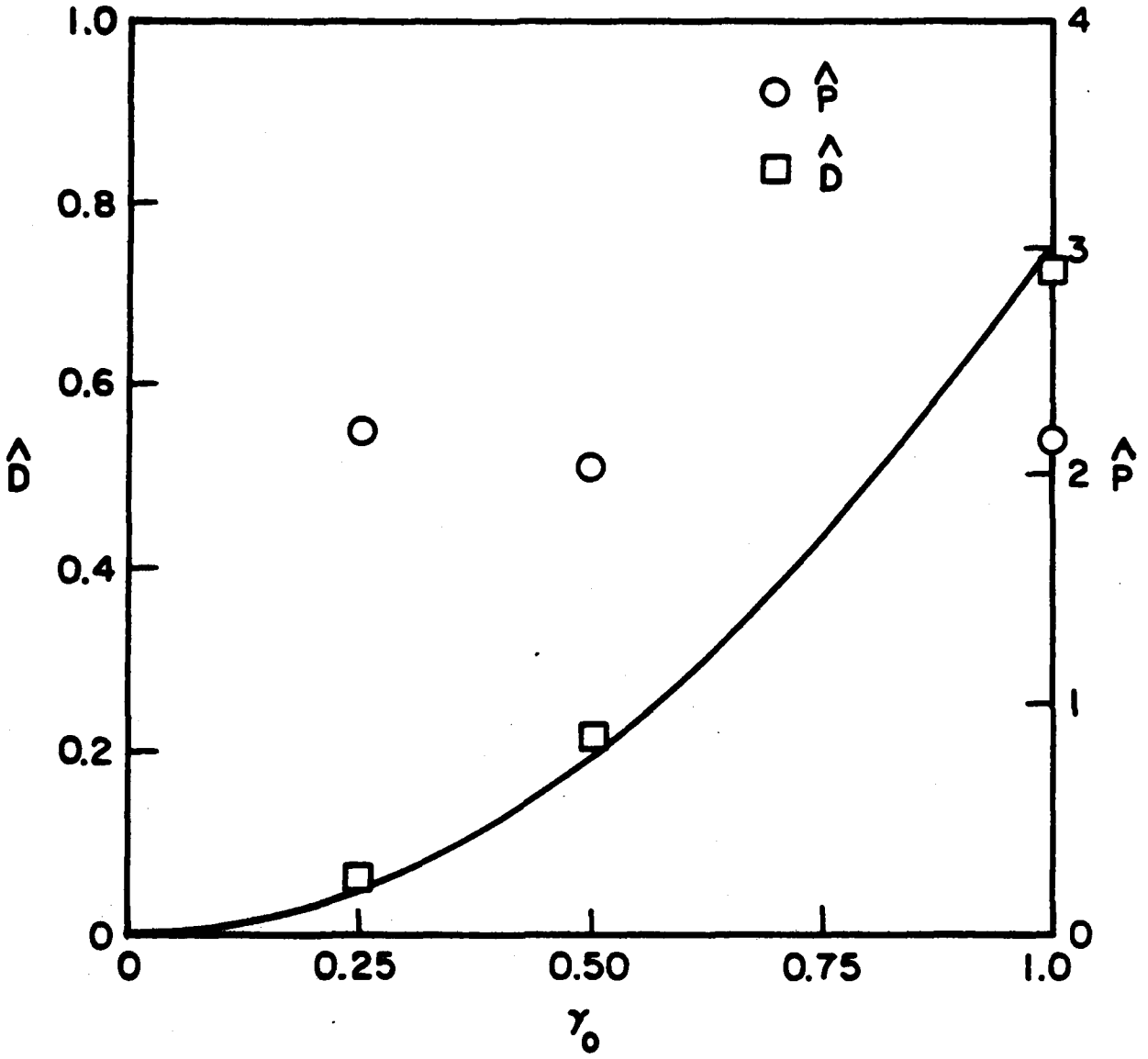

Fig. 7: The dependence of the diffusion coefficient $\hat{D}$ and the root-mean-square potential $\hat{P}$ on the ion driving term $\gamma_0 = \sqrt{\pi}\, V_{di}/v_i$ is shown for a fixed linearly unstable spectrum of waves ($\gamma_{e0}/\gamma_0 = 0.1$ and $\nu_0 = 0$). The reference curve is given by $D = 0.76\, \gamma_0^2$.

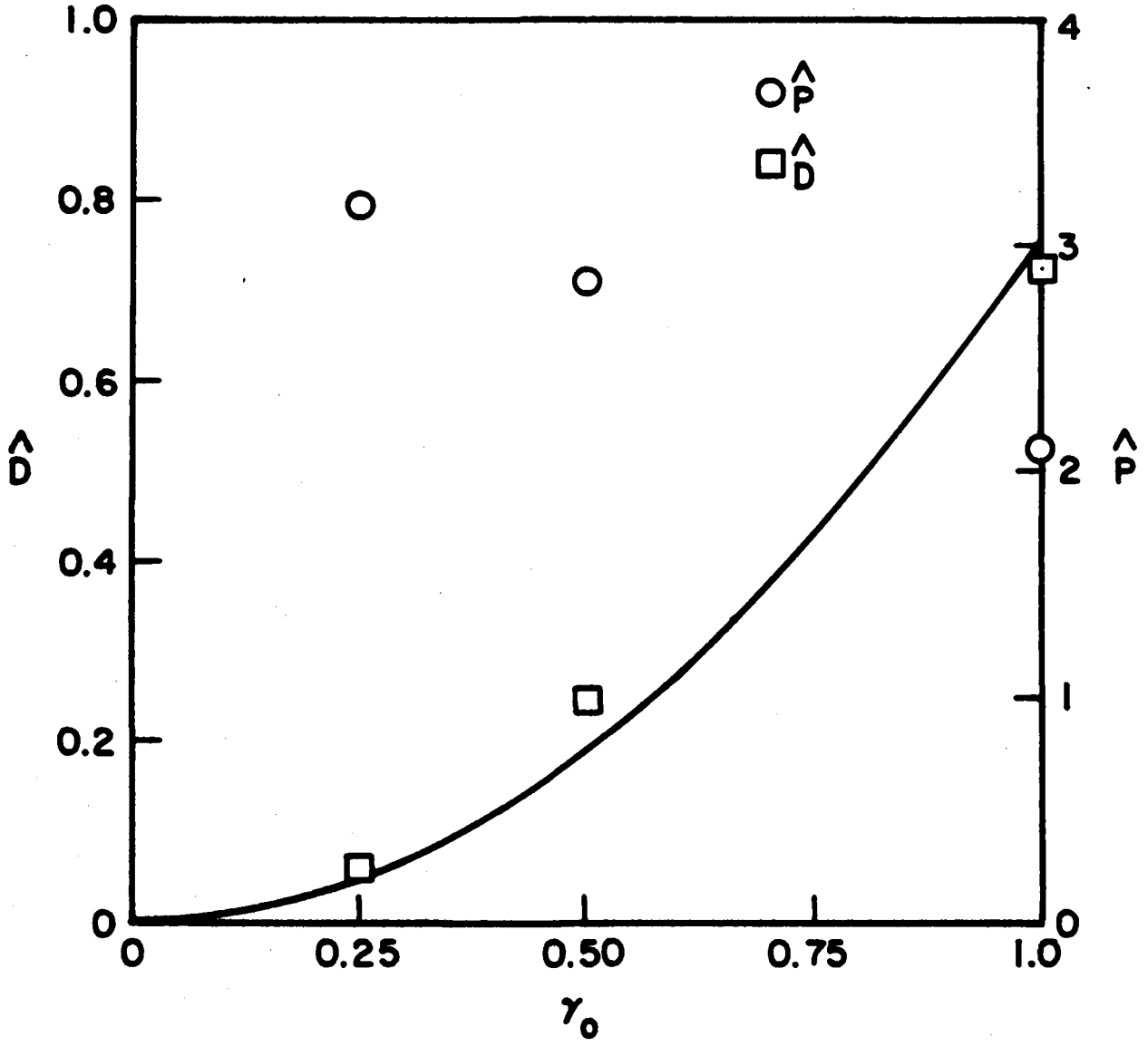

Fig. 8: The dependence of $\hat{D}$ and $\hat{P}$ on γ_0 is shown for a fixed electron VB damping rate $\gamma_{e0} = 0.11$ with $\nu_0 = 0$. The reference curve is again given by $D = 0.76\ \gamma_0^2$.

as γ_{e0} increases can be clearly seen in plots of the 2-D wave spectrum. By comparing the quasilinear diffusion coefficient in Eq. (26) with the portion of the linear growth rate in Eq. (14) which comes from the resonant ion interaction and the expression for the wave energy in Eq. (39), we find that roughly

$$\hat{D} \sim \partial W_i/\partial t,$$

where $\partial W_i/\partial t$ is the rate at which energy is extracted from the ions. Thus, our numerical results indicate that the rate at which the instability is taking energy from the ions is nearly independent of the electron damping. Of course, damped modes must always be included in the simulation or the wave energy does not saturate. The damping rate γ_{e0} must therefore remain finite.

V. Numerical Results: Collisional Damping

In laboratory and ionospheric plasmas classical damping can dominate the collisionless VB electron damping. As noted previously in Fig. 3b, collisional damping stabilizes both long and short wavelength modes and, unlike the VB resonant electron damping, can stabilize the entire spectrum. The results of our numerical computations for this case are summarized in Fig. 9 where we show the dependence of the saturated values of $\hat{D}$ and $\hat{P}$ on the collisional damping coefficient ν_0 for $\gamma_0 = 1.0$. The diffusion coefficient $\hat{D}$ and potential $\hat{P}$ are virtually independent of ν_0. This result is rather surprising because as ν_0 increases the range of unstable modes in $\underset{\sim}{k}$ space decreases dramatically (Fig. 3b) and, as a consequence, the characteristic wave spectra after saturation in the three cases presented in Fig. 9 are rather different. The spectra in the cases $\nu_0 = 0.05$ and 0.10 are similar to those presented in Sec. IV, the spectrum being somewhat broader for $\nu_0 = 0.05$ because the range of linearly unstable modes extends to larger values of $|\hat{\underset{\sim}{k}}|$. For $\nu_0 = 0.15$ the linearly unstable region of $\underset{\sim}{k}$ space has become rather localized and, as shown in Fig. 10, the saturated wave spectrum is much more peaked. The two dominant peaks at $\underset{\sim}{n} = (0, \pm 4)$ correspond to the most unstable modes while the secondary peak at $\underset{\sim}{n} = (2,0)$ is the parametrically generated daughter wave. In this case the damping of the modes with finite n_x is so large

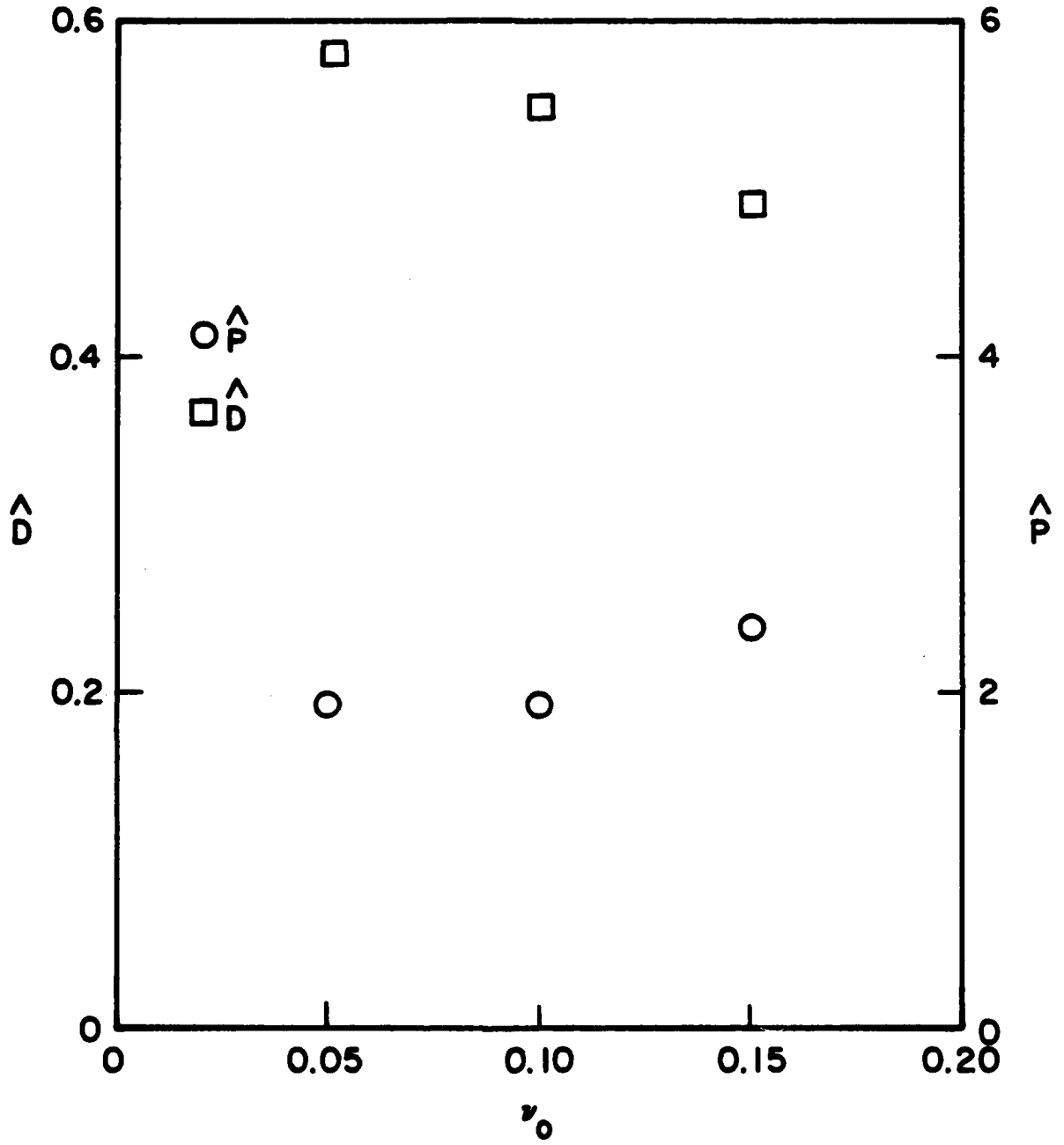

Fig. 9: The dependence of $\hat{D}$ and $\hat{P}$ on the electron collisional damping rate is shown with $\gamma_0 = 1.0$ and $\gamma_{e0} = 0$.

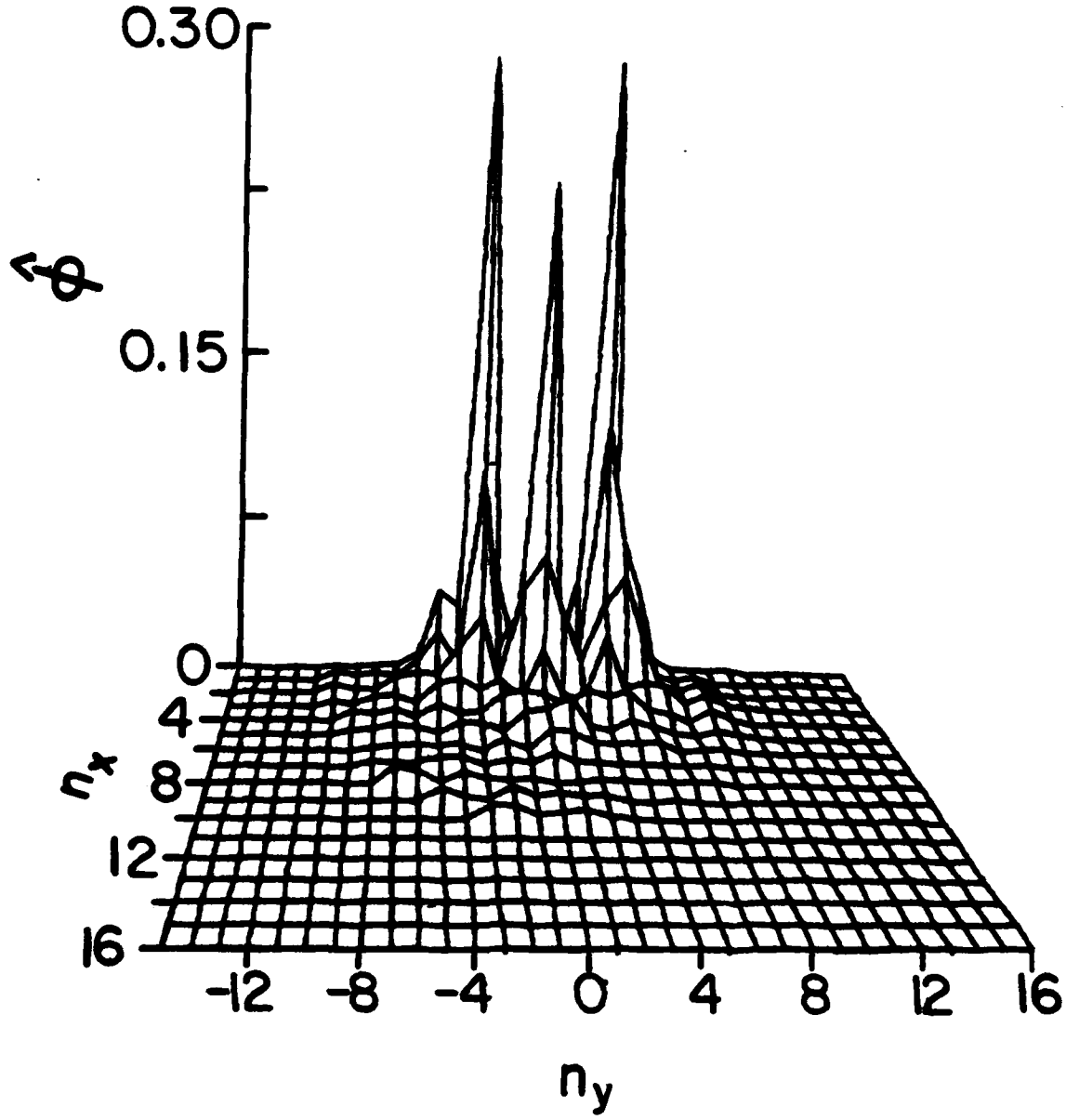

Fig. 10: The two-dimensional wave spectrum is shown for $\gamma_0 = 1.0$ and $\nu_0 = 0.15$, which is close to marginal stability.

(except for $n_y = 0$) that the energy which is pumped into them is rapidly dissipated and the wave spectrum remains quite narrow. Nevertheless, the saturated values of both $\hat{P}$ and $\hat{D}$ are virtually the same as those computed for smaller values of ν_0. This result is a consequence of the structure of the nonlinearity in Eq. (13) which only couples modes $\underset{\sim}{k}'$, $\underset{\sim}{k}$ with $\underset{\sim}{k}' \times \underset{\sim}{k} \neq 0$. For the case of a narrow wave spectrum such as that shown in Fig. 10 the coupling of the modes is quite weak. Therefore, even though the growth rates of the unstable waves are small, the coupling of wave energy to the stable modes is correspondingly very weak and the saturation amplitude remains large.

From our numerical results we conclude that the saturation of the lower-hybrid-drift instability remains large even as collisions force the mode towards marginal stability. At marginal stability, of course, $\hat{\phi} \to 0$. This rather discontinuous behavior as collisionality increases seems rather unphysical and compels us to re-evaluate our assumptions. In the Introduction we argued that ion trapping was not a viable saturation mechanism when a broad, two-dimensional wave spectrum is excited. As we approach marginal stability by increasing the collisionality, the spectrum becomes quite narrow so that ion trapping should, at some point, become effective and saturate the instability at a lower amplitude than that which we have calculated from our mode coupling theory. Ion trapping occurs when the bounce time ω_{bi}^{-1} of an ion in the wave potential becomes comparable to the growth time γ^{-1} of the instability or

$$\omega_{bi}^2 = k^2 e\phi/m_i = \gamma^2. \tag{41}$$

In our normalized units,

$$\hat{\phi} = \hat{\gamma}^2 (m_i/m_e)^{1/2} v_{di}/v_i \tag{42}$$

for $\hat{k} \sim 1$ so that $\hat{\phi} \to 0$ as the mode approaches marginal stability. Saturation by ion trapping occurs at a lower amplitude than that resulting from mode coupling when

$$\hat{\gamma} < (m_e/m_i)^{1/4} (v_i/v_{di})^{1/2}. \tag{43}$$

VI. Summary and Applications

A nonlinear wave equation [see Eq. (13)] has been derived which describes two-dimensional ($\underset{\sim}{k}\cdot\underset{\sim}{B} = 0$) lower-hybrid-drift wave turbulence in a finite β plasma. As in the linear theory of this instability in the weak drift regime, the ions are treated as unmagnetized and to lowest order respond adiabatically to the potential fluctuations. The resonant ion contribution is included as a correction to provide the driving energy for the instability. The nonlinear portion of the wave equation arises from the electrons through their $\underset{\sim}{E} \times \underset{\sim}{B}$ and polarization drifts. In addition, electron dissipation is included either through the collisionless VB resonance or through collisional viscosity.

The nonlinear wave equation has been solved numerically using a pseudo-spectral method code to obtain the evolution and saturation of the wave spectrum as well as the self-consistent particle flux. The wave energy typically saturates as the peaked unstable spectrum spreads throughout the unstable and weakly damped regions of $\underset{\sim}{k}$ space. The saturated wave spectrum is characterized by two main components: a broad, nearly isotropic spectrum with $|\underset{\sim}{k}| \gtrsim \rho_{es}^{-1}$; and a jagged spectrum consisting of narrow peaks in the range $|\underset{\sim}{k}| \sim 0.5\ \rho_{es}^{-1}$. These peaks are typically displaced towards long wavelength from the linearly most unstable waves by almost a factor of two. The peaks move around in $\underset{\sim}{k}$ space as the waves exchange energy in a dynamic fashion.

Our numerical computations demonstrate that the wave energy saturates when the nonlinearity becomes comparable to the linear frequency of the modes,

$$\frac{\partial}{\partial t} \sim \omega_k \sim \underset{\sim}{V}_e \cdot \nabla \sim kV_e \ , \tag{44}$$

where $\underset{\sim}{V}_e$ is the $\underset{\sim}{E} \times \underset{\sim}{B}$ velocity of the electrons and $\omega_k = k_y V_{di}/(1 + k^2\rho_{es}^2)$. For the most unstable modes, $k\rho_{es} \sim 1$, $\omega_k \sim V_{di}/\rho_{es} \sim \omega_{lh} V_{di}/v_i$ and (44) can be written as

$$e\phi/T_i \simeq 2\text{-}3\ (2m_e/m_i)^{1/2} V_{di}/v_i\ , \tag{45}$$

where the numerical factor comes from the detailed computations. We have also found that the saturation level is relatively insensitive to both the magnitude of the electron dissipation, as long as the damping is sufficient to stabilize the shortest wavelengths in the computational grid, and the damping (growth) rate of the long wavelength modes.

Our interpretation of the saturation amplitude in Eq. (45) is that effective energy exchange between the linearly growing and damped modes can only take place when the nonlinearity becomes sufficiently large to overcome the linear frequency mismatch

$$\Delta\omega = \omega_{k1} + \omega_{k2} + \omega_{k3} \tag{46}$$

between interacting waves, $\underset{\sim}{k}_1$, $\underset{\sim}{k}_2$ and $\underset{\sim}{k}_3$. Below the threshold given in Eq. (45), only a few modes which satisfy $\Delta\omega \simeq 0$ can exchange energy. Above this threshold all modes can exchange energy. The saturation amplitude in Eq. (45) also corresponds to the threshold for electron $\underset{\sim}{E} \times \underset{\sim}{B}$ trapping[31] so that strong mode coupling is really a consequence of the strong nonlinear behavior of the electrons during this trapping process.

The particle flux has been computed self-consistently in parallel with the nonlinear evolution of the wave spectrum. Both the exact and quasilinear expressions for the particle diffusion coefficient D are then calculated from the flux. The quasilinear expression ($D_{q\ell}$) tracks the exact expression (D) within a factor of two. To lowest order

$$D \sim \Delta x^2/\Delta t \sim \rho_{es}^2 \gamma_i \tag{47}$$

where the step size is given by $\Delta x \sim \rho_{es}$ and correlation time by $\Delta t \sim \gamma_i^{-1}$ where $\gamma_i \sim \omega_{lh}(V_{di}/v_i)^2$ is the growth rate of the most unstable mode in the absence of electron dissipation. The diffusion coefficient then becomes

$$D = 2.4\ \rho_{es}^2 (V_{di}/v_i)^2 \omega_{lh}, \tag{48}$$

where the numerical factor comes from the detailed computations. The diffusion coefficient in (48) is very insensitive to the electron dissipation, less sensitive than the saturation amplitude $e\phi/T_i$ given in Eq. (45). At first glance Eq. (47) seems to imply that the usual estimate $\gamma \sim k^2 D$ or $D \sim \rho_{es}^2 \gamma$, where γ is the maximum growth rate of the instability, is quite accurate. However, the insensitivity of D to the electron dissipation implies that this estimate is not valid. The growth rate γ decreases rather sharply as the electron dissipation is increased so that $D \sim \rho_{es}^2 \gamma$ should also decrease. It does not so that this estimate fails to reproduce the computational results.

We now compare the results of our mode coupling calculation with laboratory observations of lower-hybrid-drift wave turbulence and with the results of recent computer simulations of this instability. A CO_2 laser scattering experiment was recently carried out on the Garching, 10m θ-pinch.[5] The measured density fluctuations were flute-like ($\underset{\sim}{k} \cdot \underset{\sim}{B} \approx 0$) with clear peaks around $k_y \sim 0.5\ \rho_{es}^{-1}$. The lower-hybrid-drift instability was therefore identified as the source of these fluctuations. Our computational results are in good agreement with several prominent features of the observed wave spectra. They measure a broad angular spectrum with $k_x \lesssim k_y$. They also observe that the peak in the wave spectrum is shifted towards long wavelength by about a factor of two from the linearly most unstable mode. In the experiment data were taken for three different filling pressures, corresponding to three values of V_{di}/v_i. We have found that classical electron-ion collisions have a significant influence on the growth rate of the lower-hybrid-drift instability in this experiment especially for the two highest filling pressures. In Table I we summarize some of the parameters of their experiment including the ratio of the electron-ion collision frequency ν_{ei} to the critical collision frequency,

$$\nu_c = .814(V_{di}/v_i)^2\ \omega_{lh}$$

required to completely stabilize the lower-hybrid-drift wave. In calculating ν_{ei} we have ignored impurities by taking $Z_{eff} = 1$. The highest pressure case (8m Torr) is very close to marginal stability and, given the uncertainty in experimental parameters, could even be stable. We have completed numerical computations for the three cases given in Table I. For

Table I

Parameters of Garching Experiment

P_0(m Torr)	$n_e(10^{14}/cm^3)$	T_e(ev)	B(T)	V_{di}/v_i	$\nu_e(10^6/sec)$	ν_e/ν_c
3	1	115	.79	.52	3.3	.0067
5	2.3	74	.77	.25	13.7	.12
8	5.2	77	.73	.17	28.5	.56

the two lowest filling pressures, 3 and 5 m Torr, the instability saturates with $\tilde{n}/n = 3.4 \times 10^{-2}$ and 1.4×10^{-2}, respectively, compared with the measured values of 1.4×10^{-2} and 2.3×10^{-3}. Our calculated saturation levels are 2-3 times larger than measured experimentally. In the case of 8 m Torr the spectrum is close to marginal stability and as a consequence the saturated wave spectrum is strongly peaked around the narrow band of unstable modes at $k_y \rho_{es} \sim 0.58$. Because the spectrum is quite narrow, ion trapping cannot be neglected so that the supposition made in Ref. 5 that ion trapping saturates the instability is probably valid for this case.

A number of computer simulations of the lower-hybrid-drift instability have been carried out over the past several years.[10,13,32-34] Before comparing our results with these simulations, we would like to point out several difficulties which must be overcome in simulating this instability which are not widely recognized. The large disparity between the electron gyro time scale, Ω_e^{-1}, and the growth time of the instability, $(v_i/V_{di})^2 (m_i/m_e)^{1/2}\Omega_e^{-1}$, have forced the theorists to use artificially small mass ratios, $(m_i/m_e)^{1/2}$, and high drift velocities, V_{di}/v_i, in their codes. As a consequence, the parameter

$$\rho_{es}/L_n \sim (m_e/m_i)^{1/2}(V_{di}/v_i),$$

which should be a small number, is of order unity. Cases with larger mass ratios had to be run with larger drift velocities so ρ_{es}/L_n has not been varied significantly. The parameter ρ_{es}/L_n is significant for our computations for two reasons. First, the ratio of the rate of change of the magnetic free energy to particle drift energy in a finite β plasma scales as L_n^2/ρ_{es}^2.[15] For realistic parameters the magnetic free energy therefore greatly exceeds the drift free energy and the lower-hybrid-drift instability has no free energy bound. In the simulations this has not been the case. Second, in calculations of the nonlocal structure of the lower hybrid drift instability, it has been shown that the number of unstable harmonics in the x direction scales as L_n/ρ_{es} so that for realistic parameters a broad spectrum of unstable modes should be excited.[35] This is again not the case in many simulations. Recently, fluid-particle hybrid codes have been developed and simulations of the lower hybrid drift instability have been carried out with $\rho_{es}/L_n \ll 1$.[13] In these simulations

a broad spectrum of modes in $\underset{\sim}{k}$ space is excited with $k_x \lesssim k_y$. The cleft in the wave spectrum along $k_y = 0$, as shown in Fig. 6, is also seen in the wave spectra from these simulations. Finally, the amplitude of the potential fluctuations at saturation as obtained from these simulations is given by

$$e\phi/T_i \approx 2.4(2m_e/m_i)^{1/2}(V_{di}/v_i)^2$$

which is in excellent agreement with our results [see Eq. (45)]. One caveat to this comparison is that most of their simulations were carried out for $V_{di}/v_i \gtrsim 1$ while our theory strictly applies only for $V_{di}/v_i < 1$.

Finally, we now consider two physical systems, the earth's magnetosphere and ionosphere, where lower-hybrid-drift turbulence is expected to be important. The plasma in the neutral sheet of magnetotail is essentially collisionless. The lower-hybrid-drift instability has previously been proposed as a mechanism for dissipating magnetic energy in this reversed field configuration.[4] In the most simple 1-D model of magnetic field annihilation the flux merging velocity V_B is simply given by[15]

$$V_B = \rho_{es}^2 \nu/\lambda$$

where ν is the collision frequency (anomalous or classical) and λ is the scale length of the magnetic field. The anomalous collision frequency due to lower-hybrid-drift turbulence is given by $\nu = D/\rho_{es}^2$ so that from Eq. (48), we find

$$V_B/V_A = 2.4(m_e/m_i)^{1/2}(V_{di}/v_i)^3,$$

where $V_A^2 = B^2/4\pi m_i n$ is the Alfvén velocity. The rate of dissipation of magnetic flux is quite small during typical quiet conditions when $V_{di}/v_i \sim 0.1$ while during substorm activity when substantial thinning of the sheet has been reported ($V_{di}/v_i \lesssim 1$), the dissipation rate can be quite large.

The lower-hybrid-drift instability has also been suggested as a mechanism to generate small-scale irregularities ($\lambda \lesssim 1$ m) in the ionosphere during equatorial spread F (ESF),[21,36] and observational evidence supports this mechanism.[37,38] An important quantity to experimentalists is the power spectrum of density fluctuations during ESF.[38,39] Recently, Singh and Szuszczewicz[38] have presented a composite of ESF wave spectra from medium to short wavelengths. They find that (1) the spectra in the medium and intermediate wavelength domain ($\lambda \sim 50$ km $\rightarrow$ 200 m) scale as $k^{-1.5 \pm 0.4}$ and $k^{-2.4 \pm 0.2}$, respectively; (2) the transitional wavelengths ($\lambda \sim 200$ m $\rightarrow$ 20 m) have a $k^{-4.8 \pm 0.2}$ dependence, presumably due to drift waves; (3) the power spectrum breaks at $k\rho_i \gtrsim 1$ ($\lambda \lesssim 20$ m) to a shallower k dependence; and (4) the shortest wavelength observations ($1 \text{ m} \lesssim x \lesssim 20$ m) are consistent with a wave-particle interaction such as the lower-hybrid-drift instability. In order to apply the results of our nonlinear theory to the ionosphere we show in Fig. 11 a plot of $|\hat{\phi}_k|^2 = (e\phi/T_i)^2(v_i/V_{di})^2(m_i/2m_e)$ versus $n^2 = 9\hat{k}^2 = 9k^2\rho_{es}^2$ after saturation for $V_{di}/v_i = 0.56$ and $\nu_e/\omega_{lh} = 0.04$. Since we assume quasi-neutrality and the ions are basically adiabatic ($\delta n_i/n \sim e\phi/T_i$), Fig. 11 can be interpreted as an instantaneous power spectrum of density fluctuations associated with the lower-hybrid-drift instability. The arrow at $n^2 \sim 9$ denotes the fastest growing linear mode (for typical ionospheric parameters B ~ 0.3 G, and $T_i \sim 0.1$ ev this corresponds to $\lambda \sim 15$ cm). Two important aspects of this figure bear comment. First, there is substantial power in the long wavelength regime ($n^2 \lesssim 9$) and the spectrum is relatively flat, consistent with observational results. And second, the short wavelength spectrum ($n^2 > 9$) corresponds to a k^{-6} dependence, somewhat steeper than the transitional regime which has a $k^{-4.8}$ dependence. Thus, we predict that the very short wavelength power spectrum ($\lambda \lesssim 15$ cm) has a k^{-6} behavior. Experimentalists are unable to resolve the power spectrum of these very short wavelength modes so that our results cannot be verified at this time but await further improvements in experimental techniques.

Acknowledgments

This research has been supported by ONR and NASA. One of us (J.F.D.) was partially supported by DOE.

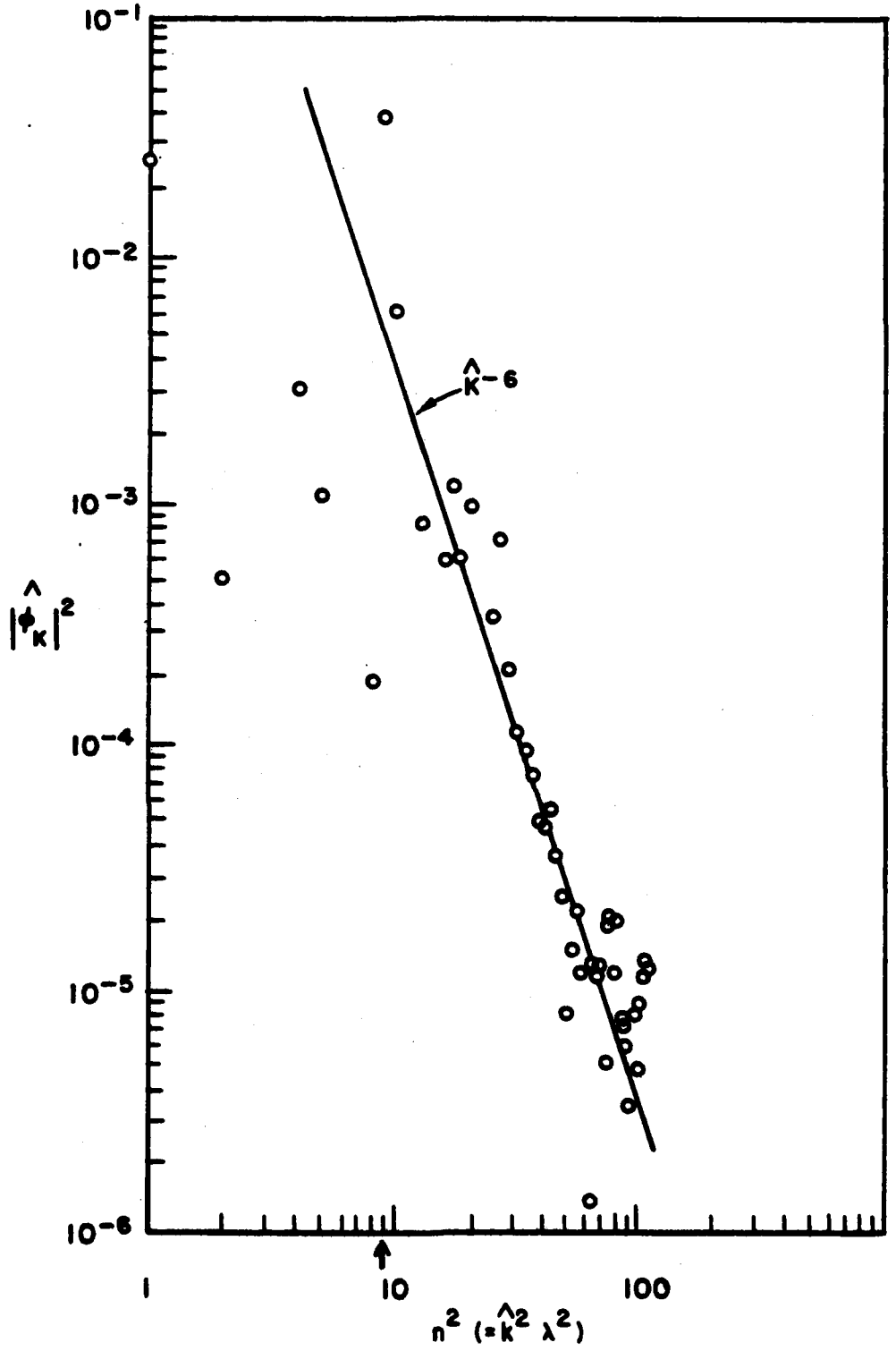

Fig. 11: The instantaneous power spectrum is shown after saturation for $V_{di}/v_i = 0.56$ ($\gamma_0 = 1.0$) and $\nu_e/\omega_{1h} = 0.04$ ($\nu_0 = 0.05$).

References

1. W.D. Davis, A.W. DeSilva, W. Dove, H.R. Griem, N.A. Krall and P.C. Liewer, in Plasma Physics and Controlled Nuclear Fusion Research (International Atomic Energy Agency, Vienna, 1971), Vol. III, p. 289.
2. R.C. Davidson, N.T. Gladd and Y. Goren, Phys. Fluids 21, 992 (1978).
3. M. Tuszewski and R.K. Linford, Phys. Fluids 25, 765 (1982).
4. J.D. Huba, N.T. Gladd and K. Papadopoulos, J. Geophys. Res., 83, 5217 (1978).
5. H.U. Fahrbach, W. Koppendorfer, M. Munich, J. Neuhauser, H. Rohr, G. Schramm, J. Sommer and E. Holzhauer, Nucl. Fusion, 21, 257 (1981).
6. R.L. McPherron, Rev. Geophys. Space Phys., 17, 657 (1979).
7. N.A. Krall and P.C. Liewer, Phys. Rev. A, 4, 2094 (1971).
8. R.C. Davidson, N.T. Gladd, C.S. Wu and J.D. Huba, Phys. Fluids 20, 301 (1977).
9. J.F. Drake, J.D. Huba and N.T. Gladd, Phys. Fluids 26, 2247 (1983).
10. D. Winske and P.C. Liewer, Phys. Fluids 21, 1017 (1978).
11. J.F. Drake and T.T. Lee, Phys. Fluids 24, 1115 (1981).
12. R.Z. Sagdeev and A.A. Galeev, Nonlinear Plasma Theory (W.A. Benjamin, Inc., New York, 1969), Ch. II, p. 37.
13. J.U. Brackbill, D.W. Forslund, K. Quest and D. Winske (private communication).
14. R.C. Davidson, Phys. Fluids 21, 1017 (1978).
15. J.F. Drake, N.T. Gladd and J.D. Huba, Phys. Fluids 24, 78 (1981).
16. S.P. Gary, Phys. Fluids 23, 1193 (1980).
17. T.H. Dupree and D.J. Tetreault, Phys. Fluids 21, 425 (1978).
18. P.H. Diamond and J.R. Myra, Phys. Fluids 26, 1481 (1983).
19. J.D. Huba and K. Papadopoulos, Phys. Fluids 21, 121 (1978).
20. J.F. Drake, P.N. Guzdar and J.D. Huba, Phys. Fluids 26, 601 (1983).
21. J.D. Huba and S.L. Ossakow, J. Geophys. Res., 86, 829 (1981).
22. A. Hasegawa and K. Mima, Phys. Fluids 21, 87 (1978).
23. W. Horton, Phys. Rev. Lett. 37, 1269 (1976).
24. R.E. Waltz, Phys. Fluids 26, 169 (1983).
25. P.W. Terry and W. Horton, Phys. Fluids 26, 106 (1983).

26. H. Hasegawa and D.G. Pettifor, Phys. Rev. Lett. 50, 130 (1983).
27. A. Hasegawa, C.G. Maclennan and Y. Kodama, Phys. Fluids 22, 2122 (1979).
28. D. Fyfe and D. Montgomery, Phys. Fluids 22, 246 (1974).
29. D. Fyfe, G. Joyce and D. Montgomery, J. Plasma Phys. 17, 317 (1977).
30. S.A. Orszag, Stud. Appl. Math. 50, 293 (1971).
31. H. Ching, Phys. Fluids 16, 130 (1973); R.E. Aamodt, Phys. Fluids 20, 960 (1977).
32. D. Winske, Phys. Fluids 24, 1069 (1981).
33. M. Tanaka and T. Sato, J. Geophys. Res. 86, 5541 (1981); Phys. Rev. Lett. 47, 714 (1981).
34. Y.-J. Chen and C.K. Birdsall, Phys. Fluids 26, 180 (1983).
35. J.D. Huba, J.F. Drake and N.T. Gladd, Phys. Fluids 23, 552 (1980); J.R. Myra, P.J. Catto and R.E. Aamondt, Phys. Fluids 24, 651 (1981).
36. J.D. Huba, P.K. Chaturvedi, S.L. Ossakow, and D.M. Towle, Geophys. Res. Lett. 5, 695 (1978).
37. W.R. Hoegy, S.A. Curtis, L.H. Brace, N.C. Maynard, and R.A. Heelis, Geophys. Res. Lett. 9, 993 (1982).
38. M. Singh and E.P. Szuszczewicz, to be published in J. Geophys. Res. (1983).
39. M.C. Kelley, R. Pfaff, K.D. Baker, J.C. Ulwick, R. Livingston, C. Rino, and R. Tsunoda, J. Geophys. Res. 87, 1575 (1982).

Appendix

One caveat needs to be added to the discussion of the mode coupling in lower-hybrid-drift turbulence presented in Sec. II. The dispersion relation in Eq. (17) was derived by keeping only the interaction of $(\hat{\omega}, \hat{k})$ with its nearest neighbors $(\hat{\omega}_{\pm}, k_{\pm})$. Unfortunately, the coupling to higher order modes $k \pm pk_0$ with $p > 1$ cannot be neglected in general. This can be most easily understood in the limit $\hat{\omega} \gg \hat{\omega}_k, \hat{\omega}_{\pm}$ [see Eq. (18)]. Since we have made no a priori assumption on k, the dispersion relation should remain invariant under the operation $k \to k \pm pk_0$. The dispersion relation in Eq. (17) does not have this property and therefore cannot be correct. In this limit there is no small parameter which allows the coupling to higher order modes to be neglected. The coupling can be cut off, however, by adding dissipation to the system. When the modes $k \pm pk_0$ (with $p > 1$) are heavily damped, the coupling to these modes can be neglected and the dispersion relation in Eq. (17) is correct. For the parameters considered in this paper, these modes are indeed heavily damped so that the dispersion relation in (17) can be justified.

DISTRIBUTION LIST

PLEASE DISTRIBUTE ONE COPY TO EACH OF THE FOLLOWING PEOPLE (UNLESS OTHERWISE NOTED)

NAVAL RESEARCH LABORATORY
WASHINGTON, D.C. 20375
Dr. P. MANGE - CODE 4101
Dr. P. GOODMAN - CODE 4180

A.F. GEOPHYSICS LABORATORY
L.G. HANSCOM FIELD
BEDFORD, MA 01730
DR. T. ELKINS
DR. W. SWIDER
MRS. R. SAGALYN
DR. J.M. FORBES
DR. T.J. KENESHEA
DR. W. BURKE
DR. H. CARLSON
DR. J. JASPERSE

BOSTON UNIVERSITY
DEPARTMENT OF ASTRONOMY
BOSTON, MA 02215
DR. J. AARONS

CORNELL UNIVERSITY
ITHACA, NY 14850
DR. W.E. SWARTZ
DR. D. FARLEY
DR. M. KELLEY

HARVARD UNIVERSITY
HARVARD SQUARE
CAMBRIDGE, MA 02138
DR. M.B. McELROY
DR. R. LINDZEN

INSTITUTE FOR DEFENSE ANALYSIS
2000 NORTH BEAUREGARD STREET
ALEXANDRIA, VA 22311
DR. E. BAUER

MASSACHUSETTS INSTITUTE OF TECHNOLOGY
PLASMA FUSION CENTER
LIBRARY, NW16-262
CAMBRIDGE, MA 02139

NASA
GODDARD SPACE FLIGHT CENTER
GREENBELT, MD 20771
DR. K. MAEDA
DR. S. CURTIS
DR. M. DUBIN
DR. N. MAYNARD - CODE 696

COMMANDER
NAVAL AIR SYSTEMS COMMAND
DEPARTMENT OF THE NAVY
WASHINGTON, D.C. 20360
DR. T. CZUBA

COMMANDER
NAVAL OCEAN SYSTEMS CENTER
SAN DIEGO, CA 92152
MR. R. ROSE - CODE 5321

NOAA
DIRECTOR OF SPACE AND ENVIRONMENTAL LABORATORY
BOULDER, CO 80302
DR. A. GLENN JEAN
DR. G.W. ADAMS
DR. D.N. ANDERSON
DR. K. DAVIES
DR. R.F. DONNELLY

OFFICE OF NAVAL RESEARCH
800 NORTH QUINCY STREET
ARLINGTON, VA 22217
DR. G. JOINER

PENNSYLVANIA STATE UNIVERSITY
UNIVERSITY PARK, PA 16802
DR. J.S. NISBET
DR. P.R. ROHRBAUGH
DR. L.A. CARPENTER
DR. M. LEE
DR. R. DIVANY
DR. P. BENNETT
DR. F. KLEVANS

SCIENCE APPLICATIONS, INC.
1150 PROSPECT PLAZA
LA JOLLA, CA 92037
DR. D.A. HAMLIN
DR. E. FRIEMAN

STANFORD UNIVERSITY
STANFORD, CA 94305
DR. P.M. BANKS

U.S. ARMY ABERDEEN RESEARCH
AND DEVELOPMENT CENTER
BALLISTIC RESEARCH LABORATORY
ABERDEEN, MD
DR. J. HEIMERL

GEOPHYSICAL INSTITUTE
UNIVERSITY OF ALASKA
FAIRBANKS, AK 99701
DR. L.E. LEE

UNIVERSITY OF CALIFORNIA,
BERKELEY
BERKELEY, CA 94720
DR. M. HUDSON

UNIVERSITY OF CALIFORNIA
LOS ALAMOS SCIENTIFIC LABORATORY
J-10, MS-664
LOS ALAMOS, NM 87545
DR. M. PONGRATZ
DR. D. SIMONS
DR. G. BARASCH
DR. L. DUNCAN
DR. P. BERNHARDT
DR. S.P. GARY

UNIVERSITY OF MARYLAND
COLLEGE PARK, MD 20740
DR. K. PAPADOPOULOS
DR. E. OTT

JOHNS HOPKINS UNIVERSITY
APPLIED PHYSICS LABORATORY
JOHNS HOPKINS ROAD
LAUREL, MD 20810
DR. R. GREENWALD
DR. C. MENG

UNIVERSITY OF PITTSBURGH
PITTSBURGH, PA 15213
DR. N. ZABUSKY
DR. M. BIONDI
DR. E. OVERMAN

UNIVERSITY OF TEXAS
AT DALLAS
CENTER FOR RESEARCH SCIENCES
P.O. BOX 688
RICHARDSON, TX 75080
DR. R. HEELIS
DR. W. HANSON
DR. J.P. McCLURE

UTAH STATE UNIVERSITY
4TH AND 8TH STREETS
LOGAN, UTAH 84322
DR. R. HARRIS
DR. K. BAKER
DR. R. SCHUNK
DR. J. ST.-MAURICE

PHYSICAL RESEARCH LABORATORY
PLASMA PHYSICS PROGRAMME
AHMEDABAD 380 009
INDIA
P.J. PATHAK, LIBRARIAN

Director
Naval Research Laboratory
Washington, D.C. 20375
ATTN: Code 4700 (26 Copies)
Code 4701
Code 4780 (100 copies)
Code 4187 (E. Szuszczewicz)
Code 4187 (P. Rodriguez)
Code 2628 (22 copies)

University of Alaska
Geophysical Institute
Fairbanks, Alaska 99701
ATTN: Library
S. Akasofu
J. Kan
J. Roederer
L. Lee

University of Arizona
Dept. of Planetary Sciences
Tucson, Arizona 85721
ATTN: J.R. Jokipii

University of California, S.D.
LaJolla, California 92037
(Physics Dept.):
ATTN: J.A. Fejer
T. O'Neil
J. Winfrey
Library
J. Malmberg
(Dept. of Applied Sciences):
ATTN: H. Booker

University of California
Los Angeles, California 90024
(Physic Dept.):
ATTN: J.M. Dawson
B. Fried
J.G. Moralles
W. Gekelman
R. Stenzel
Y. Lee
A. Wong
F. Chen
M. Ashour-Abdalla
Library
J.M. Cornwall

(Institute of Geophysics and
Planetary Physics):
ATTN: Library
C. Kennel
F. Coroniti

Columbia University
New York, New York 10027
ATTN: R. Taussig
R.A. Gross

University of California
Berkeley, California 94720
(Space Sciences Laboratory):
ATTN: Library
M. Hudson
(Physics Dept.):
ATTN: Library
A. Kaufman
C. McKee
(Electrical Engineering Dept.):
ATTN: C.K. Birdsall

University of California
Physics Department
Irvine, California 92664
ATTN: Library
G. Benford
N. Rostoker
C. Robertson
N. Rynn

California Institute of Technology
Pasadena, California 91109
ATTN: R. Gould
L. Davis, Jr.
P. Coleman

University of Chicago
Encrico Fermi Institute
Chicago, Illinois 60637
ATTN: E.N. Parker
I. Lerche
Library

University of Colorado
Dept. of Astro-Geophysics
Boulder, Colorado 80302
ATTN: M. Goldman
Library

Cornell University
School of Applied and Engineering Physics
College of Engineering
Ithaca, New York 14853
ATTN: Library
R. Sudan
B. Kusse
H. Fleischmann
C. Wharton
F. Morse
R. Lovelace

Harvard University
Cambridge, Massachusetts 02138
ATTN: Harvard College Observatory
(Library)
G.S. Vaina
M. Rosenberg

Harvard University
Center for Astrophysics
60 Garden Street
Cambridge, Massachusetts 02138
ATTN: G.B. Field

University of Iowa
Iowa City, Iowa 52240
ATTN: C.K. Goertz
D. Gurnett
G. Knorr
D. Nicholson

University of Houston
Houston, Texas 77004
ATTN: Library

University of Maryland
Physics Dept.
College Park, Maryland 20742
ATTN: K. Papadopoulos
H. Rowland
C. Wu

University of Michigan
Ann Arbor, Michigan 48140
ATTN: E. Fontheim

University of Minnesota
School of Physics
Minneapolis, Minnesota 55455
ATTN: Library
J.R. Winckler
P. Kellogg

M.I.T.
Cambridge, Massachusetts 02139
ATTN: Library
(Physics Dept.):
ATTN: B. Coppi
V. George
G. Bekefi
T. Dupree
R. Davidson
(Elect. Engineering Dept.):
ATTN: R. Parker
A. Bers
L. Smullin
(R.L.E.):
ATTN: Library
(Space Science):
ATTN: Reading Room

Princeton University
Princeton, New Jersey 08540
Attn: Physics Library
Plasma Physics Lab. Library
C. Oberman
F. Perkins
T.K. Chu
H. Okuda
V. Aranasalan
H. Hendel
R. White
R. Kurlsrud
H. Furth
S. Yoshikawa
P. Rutherford

Rice University
Houston, Texas 77001
Attn: Space Science Library
R. Wolf

University of Rochester
Rochester, New York 14627
ATTN: A. Simon

Stanford University
Institute for Plasma Research
Stanford, California 94305
ATTN: Library

Stevens Institute of Technology
Hoboken, New Jersey 07030
ATTN: B. Rosen
G. Schmidt
M. Seidl

University of Texas
Austin, Texas 78712
ATTN: W. Drummond
V. Wong
D. Ross
W. Horton
D. Choi
R. Richardson
G. Leifeste

College of William and Mary
Williamsburg, Virginia 23185
Attn: F. Crownfield

Lawrence Livermore Laboratory
University of California
Livermore, California 94551
ATTN: Library
B. Kruer
J. Thomson
J. Nucholls
J. DeGroot
L. Wood
J. Emmett
B. Lasinsky
B. Langdon
R. Briggs
D. Pearlstein

Los Alamos National Laboratory
P.O. Box 1663
Los Alamos, New Mexico 87545
ATTN: Library
D. Forslund
J. Kindel
B. Bezzerides
H. Dreicer
J. Ingraham
R. Boyer
C. Nielson
E. Lindman
L. Thode

N.O.A.A.
325 Broadway S.
Boulder, Colorado 80302
ATTN: J. Weinstock
Thomas Moore (SEL, R-43)
W. Bernstein
D. Williams

Sandia Laboratories
Albuquerque, New Mexico 87115
ATTN: A. Toepfer
G. Yeonas
D. VanDevender
J. Freeman
T. Wright

Bell Laboratories
Murray Hill, New Jersey 07974
ATTN: A. Hasegawa

Lockheed Research Laboratory
Palo Alto, California 94304
ATTN: M. Walt
J. Cladis

Physics International Co.
2400 Merced Street
San Leandro, California 94577
ATTN: J. Benford
S. Putnam
S. Stalings
T. Young

Science Applications, Inc.
Lab. of Applied Plasma Studeis
P.O. Box 2351
LaJolla, California 92037
ATTN: L. Linson
J. McBride

Goddard Space Flight Center
Greenbelt, Maryland 20771
ATTN: M. Goldstein
T. Northrop
T. Birmingham

TRW Space and Technology Group
Space Science Dept.
Building R-1, Room 1170
One Space Park
Redondo Beach, California 90278
ATTN: R. Fredericks
W.L. Taylor

National Science Foundation
Atmospheric Research Section (ST)
Washington, D.C. 20550
ATTN: D. Peacock

Goddard Space Flight Center
Code 620
Greenbelt, Maryland 20771
ATTN: Robert F. Benson

NASA Headquarters
Code EE-8
Washington, D.C. 20546
ATTN: Dr. I. Schmerling
Dr. J. Lynch
Dr. D. Butler

Klumpar, David
Center for Space Sciences
P.O. Box 688
University of Texas
Richardson, Texas 75080

Leung, Philip
Dept. of Physics
University of California
405 Hilgard Avenue
Los Angeles, California 90024

Lysak, Robert
School of Physics and Astronomy
University of Minnesota
Minneapolis, MN 55455

Schulz, Michael
Aerospace Corp.
A6/2451, P.O. Box 92957
Los Angeles, California 90009

Shawhan, Stanley
Dept. of Physics & Astronomy
University of Iowa
Iowa City, Iowa 52242

Temerin, Michael
Space Science Lab.
University of California
Berkeley, California 94720

Vlahos, Loukas
Dept. of Physics
University of Maryland
College Park, Maryland 20742

Matthews, David
IPST
University of Maryland
College Park, Maryland 20742

Schunk, Robert W.
Utah State University
Dept. of Physics
Logan, Utah 84322

END

FILMED

1-84

DTIC